Draft version July 25, 2024
Typeset using LaTeX default style in AASTeX63

JWST Reveals CO Ice, Concentrated CO_2 Deposits, and Evidence for Carbonates Potentially Sourced from Ariel's Interior

Richard J. Cartwright[a],[1] Bryan J. Holler,[2] William M. Grundy,[3,4] Stephen C. Tegler,[4] Marc Neveu,[5,6] Ujjwal Raut,[7] Christopher R. Glein,[7] Tom A. Nordheim,[1] Joshua P. Emery,[4] Julie C. Castillo-Rogez,[8] Eric Quirico,[9] Silvia Protopapa,[10] Chloe B. Beddingfield,[1] Matthew M. Hedman,[11] Katherine de Kleer,[12] Riley A. DeColibus,[8] Anastasia N. Morgan,[4] Ryan Wochner,[4] Kevin P. Hand,[8] Geronimo L. Villanueva,[6] Sara Faggi,[13,6] Noemi Pinilla-Alonso,[14] David E. Trilling,[4] and Michael M. Mueller[15]

[1] *Johns Hopkins University Applied Physics Laboratory, 11101 Johns Hopkins Rd, Laurel, MD 20723*
[2] *Space Telescope Science Institute, 3700 San Martin Drive, Baltimore, MD 21218*
[3] *Lowell Observatory, 1400 W Mars Hill Road, Flagstaff, AZ 86001*
[4] *Department of Astronomy and Planetary Science, Northern Arizona University, 527 S Beaver Street, Flagstaff AZ, 86011*
[5] *University of Maryland, 4296 Stadium Dr, College Park, MD 20742*
[6] *Solar System Exploration Division, NASA Goddard Space Flight Center, 8800 Greenbelt Road, Greenbelt, MD 20771*
[7] *Southwest Research Institute, 6220 Culebra Road, San Antonio, TX 78238-5166*
[8] *Jet Propulsion Laboratory, California Institute of Technology, 4800 Oak Grove Drive Pasadena, CA 91109*
[9] *Institut de Planétologie et d'Astrophysique (IPAG), UMR 5274, CNRS, Université Grenoble Alpes, Grenoble, France*
[10] *Southwest Research Institute, 1301 Walnut Street, Boulder, CO 80302*
[11] *Department of Physics, University of Idaho, 375 Perimeter Drive, MS 0903, Moscow ID 83843*
[12] *Division of Geological and Planetary Sciences, California Institute of Technology, 1200 E California Boulevard, Pasadena, CA 91125*
[13] *American University, 4400 Massachusetts Avenue, NW, Washington, DC 20016*
[14] *Florida Space Institute, University of Central Florida, 12354 Research Pkwy, Orlando, FL 32826*
[15] *Kapteyn Astronomical Institute Rijksuniversiteit Groningen, P.O. Box 800, 9700 AV Groningen, The Netherlands*

ABSTRACT

The Uranian moon Ariel exhibits a diversity of geologically young landforms, with a surface composition rich in CO_2 ice. The origin of CO_2 and other species, however, remains uncertain. We report observations of Ariel's leading and trailing hemispheres, collected with NIRSpec (2.87 – 5.10 μm) on the James Webb Space Telescope. These data shed new light on Ariel's spectral properties, revealing a double-lobed CO_2 ice scattering peak centered near 4.20 and 4.25 μm, with the 4.25 μm lobe possibly representing the largest CO_2 Fresnel peak yet observed in the Solar System. A prominent 4.38 μm $^{13}CO_2$ ice feature is also present, as is a 4.90 μm band that likely results from $^{12}CO_2$ ice. The spectra reveal a 4.67 μm ^{12}CO ice band and a broad 4.02 μm band that might result from carbonate minerals. The data confirm that features associated with CO_2 and CO are notably stronger on Ariel's trailing hemisphere compared to its leading hemisphere. We compared the detected CO_2 features to synthetic spectra of CO_2 ice and mixtures of CO_2 with CO, H_2O, and amorphous carbon, finding that CO_2 could be concentrated in deposits thicker than ∼10 mm on Ariel's trailing hemisphere. Comparison to laboratory data indicates that CO is likely mixed with CO_2. The evidence for thick CO_2 ice deposits and the possible presence of carbonates on both hemispheres suggests that some carbon oxides could be sourced from Ariel's interior, with their surface distributions modified by charged particle bombardment, sublimation, and seasonal migration of CO and CO_2 from high to low latitudes.

Keywords: Uranian satellites (1750); James Webb Space Telescope (2291); Surface composition (2115); Surface processes (2116); Surface ices (2117); Ice Spectroscopy (2250); Carbon dioxide (196)

Corresponding author: Richard J. Cartwright
richard.cartwright@jhuapl.edu

1. INTRODUCTION

Ariel is a candidate ocean world (e.g., Hendrix et al. 2019; Castillo-Rogez et al. 2023), with a young surface (<1 Ga in some regions; Kirchoff et al. 2022), exhibiting large chasmata and putative cryovolcanic features (e.g., Smith et al. 1986; Beddingfield & Cartwright 2021; Beddingfield et al. 2022). Ground-based telescope studies determined that the surfaces of Ariel and the other large Uranian moons are composed of H_2O ice mixed with a neutral absorber analogous to amorphous carbon (e.g., Cruikshank et al. 1977; Brown & Cruikshank 1983; Clark & Lucey 1984), overprinted by deposits of 'pure' CO_2 ice (Grundy et al. 2003, 2006; Cartwright et al. 2015, 2022), and possible ammonia (NH_3) bearing compounds (e.g., Bauer et al. 2002; Cartwright et al. 2018, 2020c, 2023; DeColibus et al. 2022, 2023).

Because of the high obliquity of the Uranus system (∼98°), the subsolar point migrates between 82°S and 82°N over the course of Uranus' orbit, exposing the summer poles of its moons to constant sunlight (estimated peak temperatures 80 – 90 K; Hanel et al. 1986; Sori et al. 2017) while blocking sunlight from reaching their winter poles (∼20 to 30 K; Sori et al. 2017), for about 21 years each season. At the estimated peak temperatures during spring and summer, CO_2 can sublimate and likely migrates to the winter hemisphere. Integrating this process over many seasons, the predicted outcome is to strip the poles of CO_2 and other volatiles and concentrate them at low latitudes, where diurnal variations in heating reduce sublimation rates (Grundy et al. 2006; Sori et al. 2017; Steckloff et al. 2022; Menten et al. 2024). Over time, CO_2 should be gradually lost to space due to Jeans escape and magnetospheric interactions, depleting surface deposits, potentially enriching heavy isotopes, and raising the possibility that CO_2 is actively replenished.

By analogy to surface irradiation of the Galilean satellites and Saturn's mid-sized moons, radiolytic generation of CO_2 and other species might occur on the Uranian satellites (Grundy et al. 2003, 2006; Cartwright et al. 2015). Such a process might explain the stronger CO_2 'triplet' band (1.9 – 2.1 μm) on the trailing hemispheres of the largest Uranian moons and its weakening with increasing orbital distance (i.e., strongest on Ariel, weakest on Oberon). Nevertheless, predictions of moon-magnetosphere interactions at Uranus are not well constrained, and perhaps CO_2 is native and sourced from these moons' interiors, with larger deposits on their trailing sides due to enhancement by radiolysis, similar to the multiple origin scenarios proposed for CO_2 on Jupiter's moon Callisto (e.g., Hibbitts et al. 2000, 2002; Moore et al. 2004a; Cartwright et al. 2024).

Irradiation of CO_2 should also generate other species, including CO (e.g., Bennett et al. 2010b; Raut et al. 2012; Raut & Baragiola 2013; Mifsud et al. 2022), carbon suboxide (C_3O_2; e.g., Strazzulla et al. 2007), and perhaps the cyanate ion (OCN^-) and other CN-bearing compounds, assuming CO_2 can interact with NH_3 and H_2O (e.g., Hudson et al. 2001). Supporting this scenario, some ground-based spectra of Ariel exhibit a 2.35 μm band, tentatively attributed to CO ice (Cartwright et al. 2022). While hitherto undetected, hydrogen peroxide (H_2O_2) may be present on Ariel, forming from irradiation of H_2O, similar to Europa (e.g., Carlson et al. 1999) and Charon (Protopapa et al. 2024). Laboratory experiments demonstrate that H_2O_2 formation is more efficient in H_2O ice mixed with a small fraction of CO_2 (<9%; Mamo et al. 2023), potentially making the Uranian moons' surfaces ideal for H_2O_2 production.

Unlike the CO_2 triplet band, subtle features between 2.12 and 2.27 μm attributed to NH_3-bearing species and ammonium salts (hereon referred to as the '2.2 μm band') do not display discernible hemispherical or orbital trends. Instead, their variable band strengths suggest association with local-scale geologic features and terrains that cannot be resolved in the available disk-integrated datasets (Cartwright et al. 2020c, 2023; DeColibus et al. 2023). If NH_3-bearing species are present, they are likely replenished over short timescales due to the predicted rapid decomposition of NH_3 by magnetospheric charged particles (∼10^6 years at Miranda; Moore et al. 2007). The short lifespan of NH_3 and the possible association between geologic features and the 2.2 μm band on Ariel could result from recent exposure of NH_3-rich deposits (Cartwright et al. 2020c). However, the ancient surface of Ariel's neighboring moon Umbriel (∼4.5 Ga; Kirchoff et al. 2022) displays 2.2 μm bands as well, raising the possibility that more refractory components are contributing, such as carbonates, phyllosilicates, and organic residues (Cartwright et al. 2023).

To investigate the nature and origin of CO_2 ice and determine whether NH_3-bearing species and other constituents are present, we measured spectra of Ariel with the NIRSpec spectrograph on the James Webb Space Telescope (JWST). These observations span an important wavelength range for detecting CO_2 and CO (4.2 – 5.0 μm), NH-bearing species (2.9 – 3.2 μm), hydrocarbons (3.2 – 3.7 μm), nitriles (4.3 – 4.8 μm), carbonates (3.9 – 4.1 μm), and H_2O_2 (∼3.51 μm).

2. DATA AND METHODS

NIRSpec Observations: As part of General Observer (GO) Program 1786, NIRSpec on JWST (Jakobsen et al. 2022; Böker et al. 2023) observed Ariel with the G395M/F290LP grating (2.87 – 5.10 μm, resolving power, R, ∼ 1000) on September 6th and 7th, 2023, when the mid-observation, subobserver longitude was near 293°W (trailing hemisphere)

and 63°W (leading hemisphere), respectively (subobserver latitude ∼64.5°N for both observations). Each observation consisted of four dithers with NIRSpec's integral field unit (IFU), for a total of ∼3,735 s (leading hemisphere) and ∼ 3,793 s (trailing hemisphere) of on-target time, using the NRSIRS2RAPID readout mode. The data were downloaded from the Mikulski Archive for Space Telescopes (10.17909/cwsn-7z50) (data reduction procedures described in Section A1).

Band Measurements: We measured the band areas and depths of detected absorption features and scattering peaks using a band measurement program that defines and divides off a local linear continuum for each feature (e.g., Cartwright et al. 2024). Depth and height measurements were made by averaging the reflectance values within ± 0.002 to 0.003 μm of a user-defined band (B_c) or peak (P_c) center, and uncertainties were computed using standard error propagation procedures (e.g., Taylor 1997). The spectral contrast for each absorption band (1 - B_d), and scattering peak (P_d - 1) was then measured. The trapezoidal rule was used to measure the area of each feature, using Monte Carlo simulations sampling the 1σ errors for data points within each feature to estimate errors (Table 1).

Comparison to Synthetic and Laboratory Spectra: We compared Ariel's spectral properties to one-layer Hapke-Mie spectral models (section A2) generated using three sets of laboratory-derived indices of refraction ('optical constants') for crystalline CO_2 ice measured at 150 K (Hansen 1997), 70 K (Gerakines & Hudson 2020), and 21 K (Quirico & Schmitt 1997a,b), and for crystalline CO ice measured at 20 K (Robert Brown, private communication; Gerakines et al. 2023). Particulate mixtures of CO_2, CO, H_2O, and amorphous C are shown in Figure A1.

We present absorbance spectra of CO + CO_2 ice mixtures measured in the Astrophysical Materials Laboratory (AML) at Northern Arizona University (NAU) (Tegler et al. 2024). These co-condensed ices were made by mixing CO and CO_2 gases at room temperature before condensing as thin films on a gold mirror held at 20 K (see Tegler et al. 2024 and Grundy et al. 2024a for more detail on laboratory procedures). We also compared the Ariel data to spectra of radiolyzed CO_2 ices processed by 100 keV protons (Raut & Baragiola 2013).

3. RESULTS AND ANALYSES

3.1. *Detected Spectral Features*

CO_2 Ice: The NIRSpec data exhibit a large scattering peak centered near 4.20 μm on Ariel's leading and trailing hemispheres, flanked by an absorption band centered near 4.27 μm, and the trailing hemisphere shows an additional peak near 4.25 μm (Figure 1). All of these features are associated with the asymmetric stretch fundamental (ν_3) mode of $^{12}CO_2$ (Figure 2). Ariel's leading and trailing sides also exhibit prominent absorption features near 4.90 μm, which corresponds to a biphonon + phonon combination mode, resulting from collective vibrations across a CO_2 ice lattice (Bini et al. 1991). Radiolytic carbon trioxide (CO_3) may provide minor contributions to the 4.90 μm feature (Figure A2). Another absorption band centered near 4.38 μm is consistent with the ν_3 mode of $^{13}CO_2$ ice. Ariel's large 4.25 μm scattering peak coincides with the wavelength range where the extinction coefficient for CO_2, k, is >1 and the refractive index, n, is <1 (Gerakines & Hudson 2020) (Figure A3), suggesting that it is the largest CO_2 ice Fresnel peak yet observed on an icy body. For comparison, JWST revealed a much smaller CO_2 Fresnel peak on Charon, shifted to ∼4.265 μm (Protopapa et al. 2024).

We calculated that 26.7% of Ariel's disk is sampled by both the leading and trailing hemisphere observations (Holler et al. 2016), with most of this overlap (18.7%) at >45°N, where CO_2 is likely depleted (Grundy et al. 2006; Sori et al. 2017; Steckloff et al. 2022; Menten et al. 2024). We also measured a suite of less prominent absorption bands that may result from CO_2, C_3O_2, carbonates, and nitriles (section A7), centered near 3.33, 4.02, 4.15, 4.30, 4.41, 4.47, and 4.59 μm (Figures 2 and A4). Other tentative CO_2 ice features that are too subtle to reliably measure are centered near 3.01, 4.84, and 4.93 μm (Figures 2, 4, and A4).

CO Ice: The NIRSpec spectra show a prominent absorption feature near 4.67 μm that is consistent with the ν_3 mode of ^{12}CO ice (e.g., Sandford et al. 1988; Bennett et al. 2010b), observed on a wide variety of trans-Neptunian objects (TNOs) and Centaurs by NIRSpec (e.g., Brown & Fraser 2023; Licandro et al. 2023; Emery et al. 2024; de Pra et al. 2024; Souza-Feliciano et al. 2024). CO ice should sublimate rapidly at Ariel's peak surface temperatures (80 – 90 K), and it is probably replenished on short timescales and perhaps complexed with a less volatile component, such as CO_2 (e.g., Sandford et al. 1988). Furthermore, Ariel's 4.67 μm feature exhibits flanking sidebands that are absent from pure CO ice (Figure 3, section 3.3). A subtle feature near 4.78 μm on Ariel's trailing hemisphere likely results from ^{13}CO (see section A7 for other interpretations). We also report $^{13}CO/^{12}CO$ isotopic ratios (section A9) and modeling of possible ^{13}C enrichment (section A10).

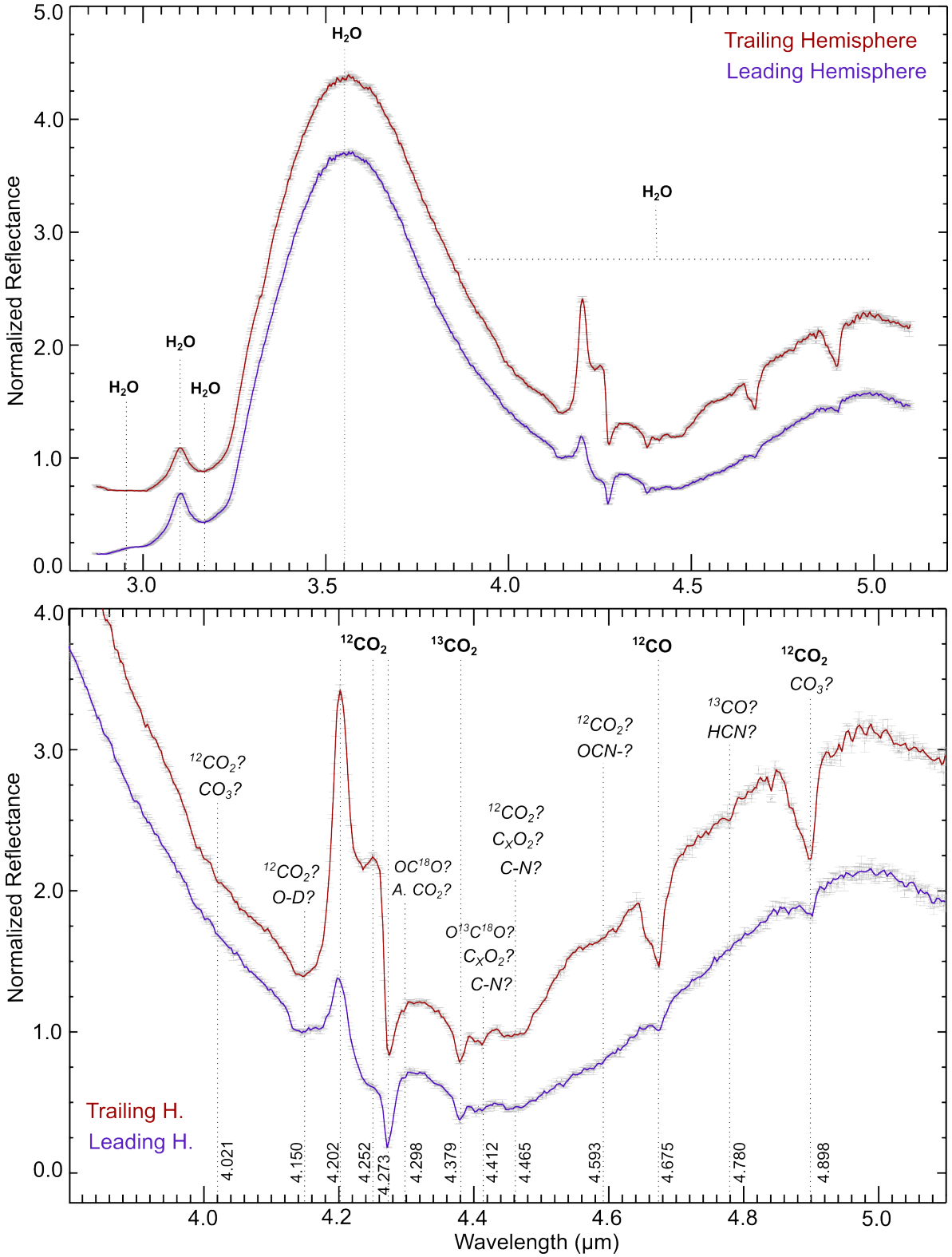

Figure 1. *Top: NIRSpec IFU (G395M/F290LP) reflectance spectra and 1σ uncertainties for Ariel's leading (purple) and trailing (red) hemispheres, vertically offset for clarity and normalized to one at 4.145 μm. Bottom: Close-up of the same spectra, focusing on the 3.8 to 5.1 μm wavelength region. Confirmed absorption bands and scattering peaks associated with H_2O ice, CO_2 ice, and CO ice are bolded, whereas suggested constituents are italicized and followed by a question mark. Amorphous CO_2 is abbreviated to 'A. CO_2.' The central wavelengths (μm) for the identified features are listed vertically along each dotted line and in Table 1.*

H_2O Ice: The spectral signature of H_2O ice is apparent on both sides of Ariel, with clear evidence for the strong 3.0 μm ν_3 mode, the 3.1 μm Fresnel peak indicative of crystalline H_2O ice, the 3.6 μm H_2O ice continuum peak, and a broad 4.5 μm $\nu_2 + \nu_R$ combination mode (Figure 1; Mastrapa et al. 2009 and references therein).

What about NH_3, Hydrocarbons, and H_2O_2? The NIRSpec spectra do not display evidence for the 2.96 μm ν_3 mode indicative of NH-bearing species nor other features associated with NH_3 or NH_4. NH-bearing features between 2.9 and 3.2 μm are also apparently absent from Charon (Protopapa et al. 2024), which exhibits a prominent 2.2 μm band long attributed to NH-bearing compounds (e.g., Brown & Calvin 2000; Buie & Grundy 2000; Grundy et al. 2016; Cook et al. 2018; Protopapa et al. 2020; Cook et al. 2023). Thus, NH-bearing species may contribute to Ariel's 2.2 μm band but are obscured by H_2O ice absorption in the 3 μm region sampled by G395M data. We also find no reliable evidence for C-H stretching modes exhibited by hydrocarbons between 3.2 and 3.5 μm, nor any evidence for a prominent H_2O_2 combination mode ($\nu_1 + \nu_6$) near 3.51 μm (Figure A5; Bain & Giguère 1955).

3.2. *Band Parameter Measurements*

We measured seven confirmed features in both spectra, and another eight likely features on Ariel's trailing hemisphere, four of which are also on Ariel's leading side (>3σ detection, Table 1). The 3.1 μm H_2O Fresnel peak is significantly stronger on Ariel's leading side. In contrast, all of the features that are definitively associated with CO_2 and CO ice are stronger on Ariel's trailing hemisphere. The distributions of H_2O and CO_2 are consistent with the hemispherical trends established in ground-based studies (e.g., Grundy et al. 2003; Cartwright et al. 2022). The features centered near 4.02, 4.41, and 4.47 μm are significantly stronger on Ariel's trailing side (>3σ difference). The 3.33 μm, 4.30 μm, 4.59 μm, and 4.78 μm bands are only reliably detected on Ariel's trailing hemisphere (>3σ detection, Table 1).

3.3. *Synthetic and Laboratory Spectra of CO_2 and CO Ice*

We compared the Ariel data to synthetic spectra of crystalline CO_2 ice (models 1-3) and CO ice (model 4), shown in Figure 2. These comparisons highlight the large number of subtle features that can be expressed by CO_2 ice (models 1 and 2), many of which appear to be present on Ariel (Table 1). Furthermore, Ariel's CO_2 scattering peaks can be approximated by a layer of large CO_2 grains ($\geq$50 μm diameters; model 3). The synthetic spectrum of CO ice matches the central wavelength positions of Ariel's 4.67 μm and 4.78 μm features (model 4), confirming the presence of this molecule and possibly confirming its heavy-carbon isotopologue.

Figure 3a shows laboratory data of CO and CO_2 mixtures, whereas Figure 3b shows CO generated in proton-irradiated CO_2 ice films containing CO and O_2, with trace amounts of CO_3 and O_3 (Raut & Baragiola 2013). The pure CO sample exhibits a narrow sideband that likely results from a longitudinal optical phonon mode (LO) caused by collective oscillations within the ice's structure. Similar LO modes have been reported for CO_2 samples illuminated at oblique angles (Cooke et al. 2016). However, this 4.658 μm sideband exhibited by Ariel's 4.67 μm feature is broader than pure CO and more similar to the sidebands exhibited by mixed CO + CO_2 samples, consistent with prior work (Sandford et al. 1988). We speculate that these sidebands result from CO dimers and trimers with vibrational frequencies distinct from monomeric CO.

The ν_3 mode in the proton-generated CO sample we analyzed is centered at shorter wavelengths ($\sim$4.668 μm) than Ariel's 4.67 μm band (4.675 μm) and does not match its sidebands (Figure 3). Similarly, another study that generated CO via electron irradiation of CO_2 (20 – 50 K) measured a band center of 4.671 μm for its ν_3 mode (Mifsud et al. 2022), slightly offset from Ariel's 4.67 μm band. Thus, radiolytic CO may not be the primary contributor to CO on Ariel. Alternatively, ice annealing processes and CO diffusion to lower energy sites in the surrounding CO_2 lattice might obscure the signature of radiolytic CO over time, making interpretation more difficult.

The other sideband ($\sim$4.687 μm) expressed by Ariel's 4.67 μm feature, is absent from pure CO ice, CO + CO_2 mixtures, and radiolytic CO, suggesting mixing with other species, including H_2O (Sandford et al. 1988) and perhaps carbonate salts. Comparison between these Ariel data and laboratory spectra of irradiated carbonates and other carbon oxides could test our inference, based on Figure 3, that CO may be (partially) native to Ariel. Similarly, new optical constants for CO + CO_2 mixtures, and CO_2 mixed with other carbon oxides, are likely required to better understand Ariel's spectral properties.

4. DISCUSSION

4.1. *Concentrated Deposits of CO_2 ice*

Table 1. Band measurements for Ariel.

Feature Name	Feature Center (μm)	Feature Wavelength Range (μm)	Hemisphere	Spectral Contrast (%)	Band Area (10^{-4} μm)	>3σ Spectral Contrast and Band Area?	Constituents (confirmed, bolded) (suggested, italicized)
[a]3.10 μm	3.100	3.014 – 3.168	Leading	99.29 ± 1.29	564.08 ± 2.07	Yes	**H_2O Ice**
			Trailing	68.37 ± 0.90	388.65 ± 1.68	Yes	
3.33 μm	3.331	3.308 – 3.362	Leading	-0.65 ± 0.68	-2.54 ± 0.63	No	*$^{12}CO_2$ Ice, CH_4, Hydrocarbons*
			Trailing	2.59 ± 0.34	5.69 ± 0.50	Yes	
4.02 μm	4.021	3.954 - 4.109	Leading	3.80 ± 0.31	35.47 ± 1.17	Yes	*$^{12}CO_2$ Ice, CO_3*
			Trailing	7.30 ± 0.66	65.38 ± 1.14	Yes	
4.15 μm	[L]4.147	4.117 – 4.187	Leading	7.33 ± 0.48	35.90 ± 0.86	Yes	*$^{12}CO_2$ Ice, O-D*
	[T]4.150	4.117 - 4.178	Trailing	9.50 ± 0.77	35.73 ± 0.67	Yes	
[a,b]4.20 μm	4.202	4.152 – 4.276	Leading	38.47 ± 0.83	[b]193.14 ± 1.61	Yes	**$^{12}CO_2$ Ice**
			Trailing	126.13 ± 1.30	743.91 ± 2.19	Yes	
[a,b]4.25 μm	4.252	4.152 – 4.276	Leading	15.64 ± 0.85	193.14 ± 1.61	Yes	**$^{12}CO_2$ Ice**
			Trailing	82.42 ± 1.10	743.91 ± 2.19	Yes	
[c]4.27 μm	4.273	4.257 – 4.303	Leading	25.86 ± 1.21	43.45 ± 0.91	Yes	**$^{12}CO_2$ Ice**
			Trailing	41.24 ± 0.79	89.45 ± 0.79	Yes	
[d]4.30 μm	4.298	4.292 – 4.302	Leading	3.22 ± 1.43	1.35 ± 0.52	No	*$^{16}O^{12}C^{18}O$ Ice, amorphous CO_2*
			Trailing	4.13 ± 0.87	1.59 ± 0.34	Yes	
4.38 μm	4.379	4.365 – 4.391	Leading	7.82 ± 0.93	10.81 ± 0.68	Yes	**$^{13}CO_2$ Ice**
			Trailing	11.12 ± 1.04	16.19 ± 0.61	Yes	
4.41 μm	[L]4.403	4.395 – 4.423	Leading	2.96 ± 0.88	3.20 ± 0.56	Yes	*$^{16}O^{13}C^{18}O$ Ice, C_XO_2, Nitriles*
	[T]4.412	4.393 – 4.429	Trailing	5.26 ± 1.13	8.38 ± 0.71	Yes	
4.47 μm	4.465	4.430 – 4.495	Leading	2.66 ± 0.86	10.22 ± 1.05	Yes	*$^{12}CO_2$ Ice, C_XO_2, Nitriles*
			Trailing	6.11 ± 0.63	27.06 ± 1.04	Yes	
4.59 μm	4.593	4.552 – 4.639	Leading	1.53 ± 0.60	6.08 ± 1.24	No	*$^{12}CO_2$ Ice, OCN^-*
			Trailing	2.50 ± 0.73	14.90 ± 1.02	Yes	
4.67 μm	4.675	4.640 – 4.706	Leading	6.60 ± 1.09	11.64 ± 1.03	Yes	**^{12}CO Ice**
			Trailing	23.29 ± 0.76	63.06 ± 0.93	Yes	
4.78 μm	4.780	4.764 – 4.795	Leading	1.70 ± 0.65	0.35 ± 0.57	No	*^{13}CO Ice, HCN*
			Trailing	2.42 ± 0.25	4.17 ± 0.78	Yes	
4.90 μm	4.898	4.845 – 4.927	Leading	4.59 ± 0.76	11.57 ± 1.30	Yes	**$^{12}CO_2$ Ice,**
			Trailing	20.29 ± 0.96	64.77 ± 1.06	Yes	*CO_3*

[a] *Spectral features are peaks measured above the continuum.*
[b] *Band areas for the 4.20 μm and 4.25 μm features are convolved, and we report the same band area for both peaks.*
[c] *The 4.27 μm feature overlaps the wavelength range of the 4.25 μm scattering peak, and the reported measurements for this feature (and its hemispherical asymmetry) are provided for completeness but are likely inaccurate.*
[d] *4.30 μm feature is partly embedded in the long-wavelength wing of the 4.27 μm feature.*
[L] = *Leading*, [T] = *Trailing.*

The results presented here and in prior studies (Grundy et al. 2003, 2006; Cartwright et al. 2015, 2020a) indicate that CO_2 on Ariel has remarkably similar spectral properties to crystalline CO_2 ice measured in the laboratory (i.e., CO_2 molecules primarily bonded to each other in a long-range order). Comparison to synthetic spectra of crystalline CO_2 ice (Figure 2) highlights that Ariel exhibits many subtle CO_2 features outside of the strong ν_3 mode. Specifically, features near 3.01, 3.33, 4.84, 4.90, and 4.93 μm on Ariel's trailing hemisphere do not appear on many other objects where CO_2 has been detected by JWST/NIRSpec (e.g., Villanueva et al. 2023; Brown & Fraser 2023; Pinto et al. 2023; Bockelee-Morvan et al. 2024; Cartwright et al. 2024; Emery et al. 2024; Wong et al. 2024; de Pra et al. 2024; Protopapa et al. 2024) (TNO examples provided in Figure A6), with the exception of Triton (Wong et al. 2023). Consequently, Ariel's surface exhibits some of the most CO_2-rich deposits in the Solar System.

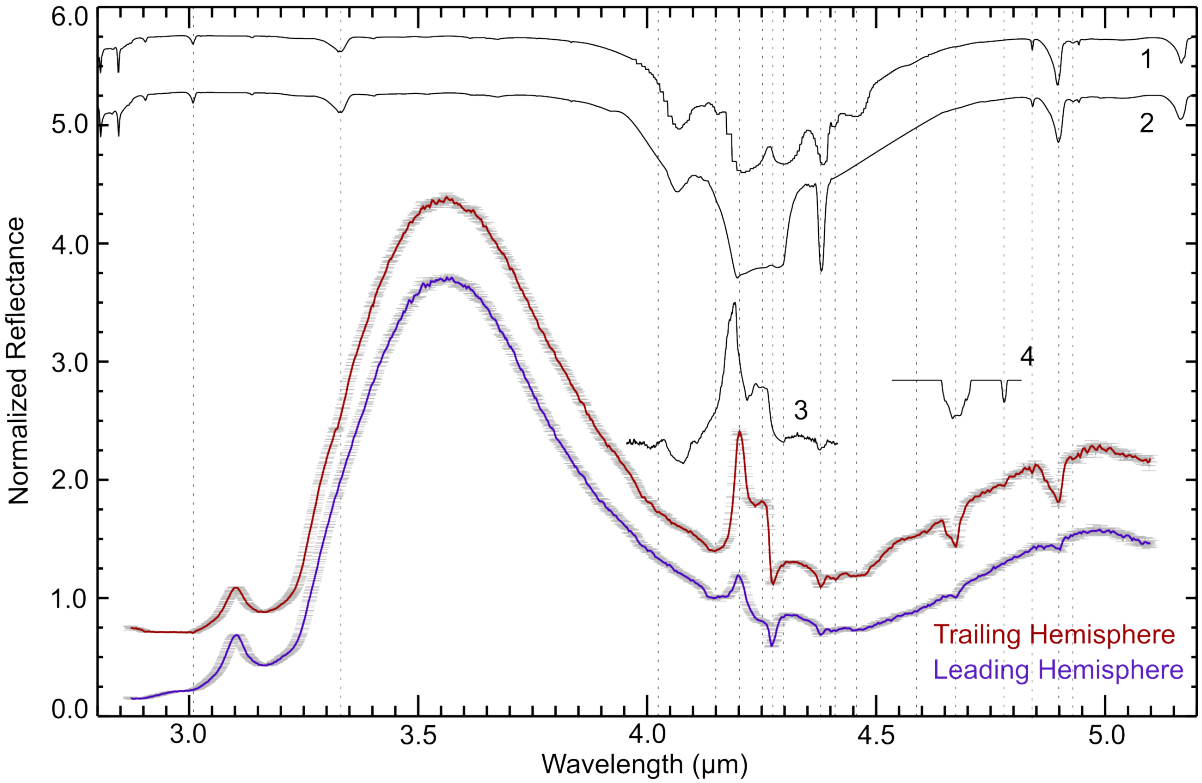

Figure 2. *Comparison between Ariel's leading (purple) and trailing (red) hemisphere spectra (vertically offset for clarity, normalized to unity at 4.145 μm) and 1σ uncertainties, along with synthetic spectra of crystalline CO_2 ice (1-3) and CO ice (4). These synthetic spectra were generated using optical constants: model 1, 10 μm grain size, Hansen (1997); model 2, 10 μm grain size, Quirico & Schmitt (1997a,b); model 3, 50 μm grain size, Gerakines & Hudson (2020); model 4, 10 μm grain size, Robert Brown (private communication).* Models 1 and 2 were scaled to the depth of the 4.90 μm band on Ariel's trailing side, Model 3 was scaled to the height of the 4.20 μm scattering peak on Ariel's trailing side, and Model 4 was scaled to the depth of the 4.67 μm band on its trailing side. All four models are offset vertically for clarity. The central wavelength of measured features (Table 1) and possible features near 3.01, 4.84, and 4.93 μm are indicated by dotted lines.

To estimate the thickness of Ariel's CO_2 ice deposits, we calculated the e-folding depths ($1/\alpha$; where α is the absorption coefficient) for near-infrared (NIR) photons propagating through a slab of CO_2 ice, which is essentially an application of the Beer-Lambert absorption law. To account for scattering off grain boundaries, we calculated the mean optical path length, MOPL = $-1/(\alpha^*\ln(R))$; where R is the reflectance; Clark & Roush 1984), using synthetic spectra composed of CO_2 ice grains (1, 10, and 100 μm diameters). The results of these two approaches indicate that photons spanning the wavelength range of the CO_2 ν_3 band (4.1 – 4.4 μm) can travel 0.0001 to 0.1 mm into slabs of CO_2 ice or deposits dominated by CO_2 grains before being absorbed (Figure 4). In contrast, photons penetrate >0.3 mm in the wavelength range of the 4.90 μm band, 4 mm in the wavelength ranges of the 3.33 and 4.84 μm bands, and upwards of 10 mm in the wavelength ranges of the possible 3.01 and 4.93 μm features (Figure 4). The penetration depth estimates reported here are broadly consistent with prior estimates made on weak CO_2 features between 1.5 to 1.7 μm (4 – 30 mm depths) and 1.9 to 2.1 μm (0.07 – 0.4 mm depths) (Cartwright et al. 2015, 2022). Additionally, these estimates are consistent with laboratory measurements of CO_2 ice optical constants, which used thin films (0.25 – 3 μm thick) to avoid saturation while measuring the ν_3 mode (Gerakines & Hudson 2020) and samples >10 mm thick to measure weaker CO_2 features (Hansen 1997, 2005).

As an additional test, we generated synthetic spectra composed of CO_2 in particulate mixtures with CO, H_2O, and amorphous carbon, finding that the CO_2 ν_3 mode is present in all mixtures (see section A2 for model details). In contrast, weak features near 3.01, 3.33, 4.84, and 4.93 μm are not present in any of these particulate mixture models, while the 4.90 μm band is present in particulate mixture models that include 40% CO_2 (Figure A1). These results support the hypothesis that CO_2 ice on Ariel's surface is segregated from H_2O ice. Whether these CO_2-

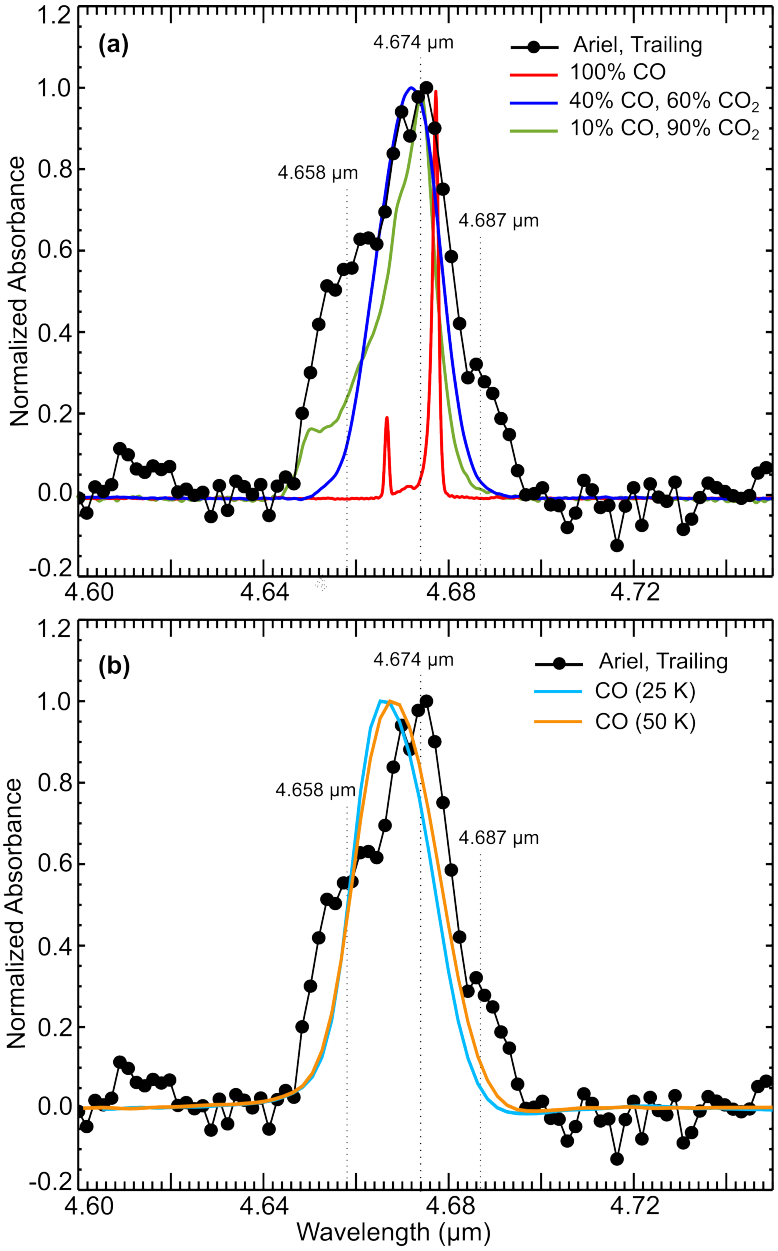

Figure 3. *(a) Comparison between a continuum-removed version of the 4.67 μm absorption band on Ariel's trailing hemisphere (black, converted into absorbance units) and laboratory absorbance spectra of pure CO ice and CO + CO_2 ice mixtures measured in the Astrophysical Material Laboratory at temperatures between 20 to 30 K, with the CO feature persisting at temperatures up to 80 K in the mixed CO + CO_2 samples (Tegler et al. 2024; Grundy et al. 2024a). Pure CO_2 ice is essentially featureless in this wavelength range and omitted for clarity. The CO_2:CO mixture (9:1, green, centered near 4.674 μm) provides a good match to the central wavelength of Ariel's 4.67 μm band, whereas mixtures with comparable amounts of CO_2 and CO (6:4, blue, centered near 4.672 μm) provide less ideal matches. Pure CO ice (red, 4.677 μm) is much narrower, offset to longer wavelengths, and exhibits a narrow sideband (4.667 μm), likely resulting from a longitudinal optical phonon mode, which does not match the broad short-wavelength sideband of Ariel's 4.67 μm band. Neither the pure CO nor CO + CO_2 mixtures are able to match Ariel's long-wavelength sideband centered near 4.69 μm. (b) Comparison between a continuum-removed version of the 4.67 μm band on Ariel's trailing hemisphere (black) and laboratory spectra of a sample dominated by CO ice generated via irradiation of a CO_2 thin film with 100 KeV H^+ protons at 25 K (light blue) and 50 K (orange), shown in optical depth units ($-\ln(R/R_0)$, where R is the reflectance of the film and gold substrate and R_0 is the reflectance of the bare gold substrate (Raut & Baragiola 2013)). All spectra are normalized to one at their maxima. The radiolytic CO features do not provide good matches to the central position, width, or sidebands of Ariel's 4.67 μm band.*

dominated deposits are spatially associated with specific geologic landforms, or are more regionally dispersed, cannot be determined with these disk-integrated spectra.

4.2. *Radiolytic Production and Seasonal Migration of CO and CO_2*

At winter temperatures of 20 to 30 K, CO_2 and CO ices are stable and likely form a winter cap. Once exposed to sunlight in spring, CO_2 and CO should start to sublimate and migrate to cold traps near the new winter pole or leave the surface environment via Jeans escape, in particular for the more volatile CO. **Seasonal migration of CO_2 molecules could lead to the formation of a transient layer of pure CO_2 frost that is predicted to be up to 2.4 mm thick (Steckloff et al. 2022). Scattering within such a thick layer of seasonally-mobile CO_2 grains might contribute to Ariel's large 4.20 μm and 4.25 μm scattering peaks. Furthermore, the JWST/NIRSpec results presented here indicate that CO_2 ice deposits could be upwards of 10 mm thick on Ariel's trailing hemisphere (section 4.1), raising the possibility that CO_2 deposits on its trailing side are resistant to seasonal migration. On Ariel's leading hemisphere, CO_2 deposits may be only ∼0.3**

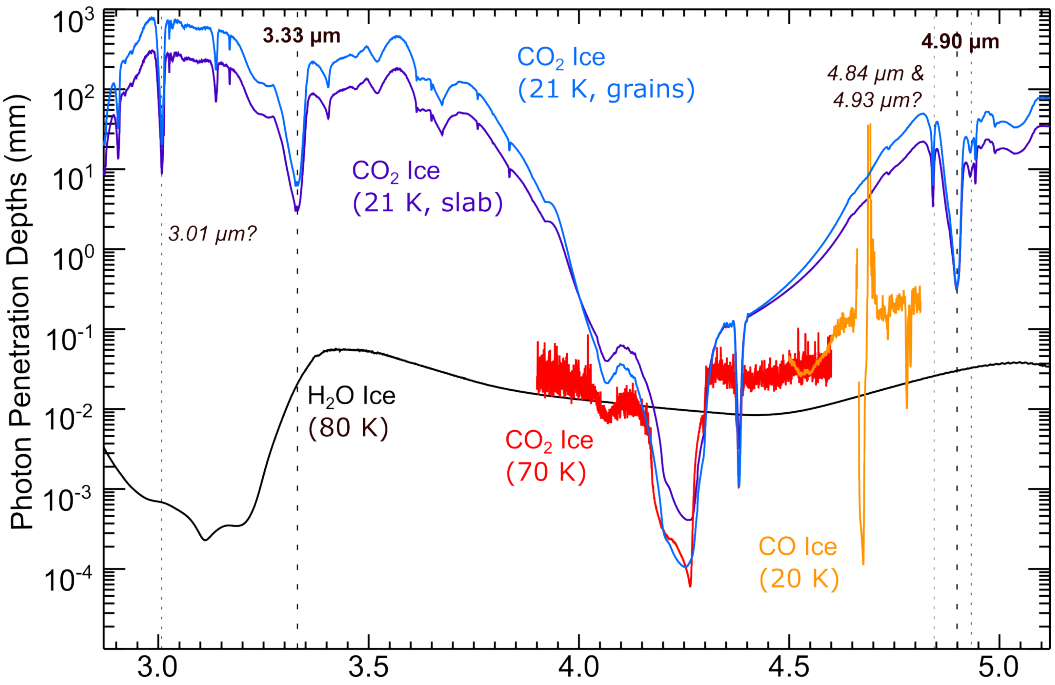

Figure 4. *e-folding photon penetration depths into a slab of CO_2 ice (red; Gerakines & Hudson 2020, purple; Quirico & Schmitt 1997a,b), CO ice (orange; Gerakines et al. 2023), and H_2O ice (black; Mastrapa et al. 2009), and mean optical path length (MOPL) for photons into a layer of CO_2 ice grains with 1 μm diameters (blue). The MOPL for photons into layers composed of 10 and 100 μm diameter CO_2 ice grains are intermediate between the blue and purple lines. The black dashed lines highlight the band centers for Ariel's 3.33 μm and 4.90 μm bands, and the gray dashed lines highlight other subtle CO_2 ice features that may be present in the spectrum of Ariel's trailing hemisphere (centered near 3.01, 4.84, and 4.93 μm). This plot shows that only the strong ν_3 modes for $^{12}CO_2$, $^{13}CO_2$, ^{12}CO, and ^{13}CO should be exhibited by Ariel, if carbon oxides are well mixed with H_2O on its surface. The presence of weaker CO_2 ice features supports the presence of concentrated CO_2 ice deposits exposed on Ariel's surface (likely mixed with small amounts of CO and perhaps other carbon oxides).*

mm thick (Figure 4), suggesting that CO_2 on its leading side could primarily result from sublimation and transport from its trailing hemisphere.

One way to explain how Ariel retains CO is if it forms at depth via radiolytic decomposition of thick CO_2 deposits. Measurements made by Voyager 2 indicate that heavy ions are largely absent from Uranus' magnetosphere (Ness et al. 1986), suggesting that high-energy electrons and protons could be the primary drivers of radiolytic processes. Energy deposition by protons and heavy ions is mostly limited to the top 0.01 mm of icy regoliths (e.g., Delitsky & Lane 1998), but energetic electrons (∼1 MeV) can penetrate cm-scale depths into ices (e.g., Nordheim et al. 2017). CO molecules generated at depth would be stable at Ariel's winter pole before diffusing out of its regolith once exposed to sunlight, possibly being retained long enough to be detected. However, geologic sources of native CO could be contributing as well (Figure 3, section 3.3).

4.3. *Possible Internally-Derived Materials*

The 2.2 μm bands detected in ground-based observations of the Uranian moons have been attributed to potentially internally-derived deposits rich in NH_3-hydrates and NH_3 ice, carbonates, phyllosilicates, and/or organics (e.g., Cartwright et al. 2020c, 2023; DeColibus et al. 2023). Although we did not detect evidence of NH-bearing species, phyllosilicates, or hydrocarbons in the G395M data, Ariel's 4.02 μm feature could result from a $\nu_1 + \nu_3$ combination mode expressed by CO_3 in carbonate minerals (Hexter 1958; Bishop et al. 2021), similar to Callisto's 4.02 μm band (Johnson et al. 2004; Cartwright et al. 2024). Laboratory experiments showed that although a 4.89 μm feature formed in irradiated CO_2 ice, attributed to radiolytic CO_3 (Figure A2; Raut & Baragiola 2013), a complementary 4 μm band was not observed. Similarly, carbonic acid (H_2CO_3), generated via irradiation of H_2O and CO_2 mixtures at cryogenic temperatures (<100 K), exhibits a broad absorption band between 3.8 and 3.9 μm (e.g., Moore & Khanna 1991; Hage et al. 1998; Gerakines et al. 2000), but it is uncertain what processes might cause this feature to shift to

longer wavelengths, matching Ariel's 4.02 μm band. It therefore seems more likely that non-radiolytic, native species contribute to Ariel's 4.02 μm band.

A prior study suggested Umbriel's 2.2 μm band may result from thermonatrite ($Na_2CO_3 \cdot H_2O$), possibly contributing to bright crater floor deposits (Cartwright et al. 2023), along with cold-trapped CO_2 ice (Sori et al. 2017). In this scenario, emplaced carbonates could serve as base material for radiolytic CO_2, or perhaps endogenic CO_2 could be delivered from Ariel's interior with carbonates, either at present or in the geologic past. Indeed, it is predicted that within deep oceans evolved from carbon-rich ices, a large fraction of CO_2 (several 100s of mmol/(kg H_2O)) may be in solution with bicarbonate (Castillo-Rogez et al. 2022). If CO_2 is outgassed from Ariel's interior, then some of it should condense and contribute to the concentrated CO_2 ice deposits detected in JWST and ground-based datasets. Endogenic CO_2, if mixed with liquid H_2O and coexisting with bicarbonate, could indicate a mildly acidic ocean (pH ~6-8), favoring the surface precipitation of bicarbonate salts and potentially Mg or Ca carbonates at lower pH values (e.g., Glein et al. 2015; Tosi et al. 2024). Alternatively, radiolytic CO_2, or native CO_2 sequestered in Ariel's crust, would permit a more basic ocean chemistry (pH > 9-10), supporting Na and NH_4 carbonate precipitation.

The presence of carbonates would have important implications for minerals possibly formed in an aqueous environment and for the habitability of Ariel's interior, including the availability of phosphorus (Postberg et al. 2023), a key chemical component for life. Except for NH_4 carbonates, carbonate salts require environments where silicate minerals can interact with liquid H_2O (Castillo-Rogez et al. 2022). Such formation environments may exist at rock-water interfaces in ocean world interiors such as Ceres, whose strong 4 μm band results from carbonates (e.g., Rivkin et al. 2006), including Na_2CO_3 salts (e.g., De Sanctis et al. 2016; Carrozzo et al. 2018; Raponi et al. 2019), likely formed from the alteration of rock in contact with an ocean that included NH_3 (Castillo-Rogez et al. 2018). **Similarly, Enceladus' plume particles are dominated by H_2O ice mixed with minor amounts of Na carbonates (Postberg et al. 2009) and Na phosphates (Postberg et al. 2023) that likely formed in its ocean.**

If CO is internally-derived and released during winter, it could persist on Ariel's surface, condensing with CO_2. To survive in Ariel's interior, endogenic CO would need to be sequestered in its crust and unable to interact with liquid H_2O, or else it would have oxidized to CO_2 or reduced to metastable organic compounds, such as formic acid/formate and perhaps CH_4 (Neveu et al. 2015; Glein & Waite Jr 2018). CO trapped as guest molecules in clathrates, however, would be more resistant to these processes and might persist. CO clathrates exhibit a ^{12}CO ν_3 mode near 4.685 μm (Dartois 2011), potentially matching a sideband on Ariel's 4.67 μm feature (Figure 3). Furthermore, the detection of CO in Enceladus' plume material (e.g., Peter et al. 2024) demonstrates that CO can survive in warm icy satellite interiors.

5. SUMMARY AND CONCLUSIONS

We analyzed JWST/NIRSpec spectral observations collected over Ariel's leading and trailing hemispheres, revealing the presence of crystalline CO_2 ice and CO ice mixed with CO_2. We detected a suite of other spectral features that might result from carbonates, C_3O_2, and nitriles. The detected CO_2 ice is likely concentrated in thick deposits, possibly mixed with a small amount of CO, but the physical state of these deposits and whether they are associated with geologic conduits to Ariel's interior, is difficult to determine with these disk-integrated spectra. Spatially-resolved NIR spectra collected by an orbiter making close flybys of the Uranian moons is required to explore the spatial relationship between volatiles and geologic features and confirm whether some carbon oxides originate in Ariel's interior (e.g., Beddingfield et al. 2020; Cartwright et al. 2021; Leonard et al. 2021; Cohen et al. 2022; National Academies of Sciences, Engineering, and Medicine 2022).

We found no compelling evidence for NH-bearing species, hydrocarbons, or H_2O_2 in the G395M data, although NH-bearing species could be present but obscured by strong 3 μm H_2O ice absorption. The lack of hydrocarbon features suggests that amorphous carbon dominates the low albedo material that is well-mixed with H_2O ice in the Uranian moons' regoliths, possibly also mixed with some 'amorphous silicates' (Cartwright et al. 2018). The apparent absence of H_2O_2 suggests that the irradiation environment at Ariel may be fairly quiescent, or extensive CO_2 deposits limit interactions between charged particles and underlying H_2O ice.

6. ACKNOWLEDGMENTS

This work is based [in part] on observations made with the NASA/ESA/CSA James Webb Space Telescope. The data were obtained from the Mikulski Archive for Space Telescopes at the Space Telescope Science Institute, which is operated by the Association of Universities for Research in Astronomy, Inc., under NASA contract NAS 5-03127

for JWST. These observations are associated with GO program 1786. Support for GO program 1786 was provided by NASA through a grant from the Space Telescope Science Institute, which is operated by the Association of Universities for Research in Astronomy, Inc., under NASA contract NAS 5-03127.

REFERENCES

Alexander, C. O., Fogel, M., Yabuta, H., & Cody, G. 2007, Geochimica et Cosmochimica Acta, 71, 4380

Applin, D. M., Izawa, M. R., & Cloutis, E. A. 2016, Icarus, 278, 7

Bain, O., & Giguère, P. A. 1955, Canadian Journal of Chemistry, 33, 527

Bauer, J. M., Roush, T. L., Geballe, T. R., et al. 2002, Icarus, 158, 178

Beddingfield, C., Li, C., Atreya, S., et al. 2020, arXiv preprint arXiv:2007.11063

Beddingfield, C. B., & Cartwright, R. J. 2021, Icarus, 114583

Beddingfield, C. B., Cartwright, R. J., Leonard, E., Nordheim, T., & Scipioni, F. 2022, The Planetary Science Journal, 3, 106

Bennett, C., Jones, B., Knox, E., et al. 2010a, The Astrophysical Journal, 723, 641

Bennett, C. J., Jamieson, C. S., & Kaiser, R. I. 2010b, Physical Chemistry Chemical Physics, 12, 4032

Bini, R., Salvi, P., Schettino, V., & Jodl, H.-J. 1991, Physics Letters A, 157, 273

Bishop, J., King, S., Lane, M., et al. 2021, Earth and Space Science, 8, e2021EA001844

Bisschop, S., Fuchs, G., Boogert, A., van Dishoeck, E., & Linnartz, H. 2007, Astronomy & Astrophysics, 470, 749

Bockelee-Morvan, D., Lellouch, E., Poch, O., et al. 2024, Astronomy & Astrophysics, 681, A27

Bohlin, R. C., & Landolt, A. U. 2015, The Astronomical Journal, 149, 122

Bohren, C., & Huffman, D. 1983, Wiley, New York

Böker, T., Beck, T., Birkmann, S., et al. 2023, Publications of the Astronomical Society of the Pacific, 135, 038001

Brown, M. E., & Calvin, W. M. 2000, Science, 287, 107

Brown, M. E., & Fraser, W. C. 2023, The Planetary Science Journal, 4, 130

Brown, R. H., & Cruikshank, D. P. 1983, Icarus, 55, 83

Buie, M., & Grundy, W. 2000, Icarus, 148, 324

Bushouse, H., Eisenhamer, J., Dencheva, N., Davies, J., & Greenfield, P. e. a. . 2023, Zenodo, zenodo.org/records/8067394

Carlson, R., Anderson, M., Johnson, R., et al. 1999, Science, 283, 2062

Carlson, R. W. 1999, Science, 283, 820

Carrozzo, F. G., De Sanctis, M. C., Raponi, A., et al. 2018, Science advances, 4, e1701645

Cartwright, R., Beddingfield, C., Nordheim, T., et al. 2021, Planetary Science Journal, 2, 120

Cartwright, R. J., DeColibus, R. A., Castillo-Rogez, J. C., et al. 2023, The Planetary Science Journal, 4, 42

Cartwright, R. J., Emery, J. P., Grundy, W. M., et al. 2020a, Icarus, 338, 113513

Cartwright, R. J., Emery, J. P., Pinilla-Alonso, N., et al. 2018, Icarus, 314, 210

Cartwright, R. J., Emery, J. P., Rivkin, A. S., Trilling, D. E., & Pinilla-Alonso, N. 2015, Icarus, 257, 428

Cartwright, R. J., Nordheim, T. A., Cruikshank, D. P., et al. 2020b, The Astrophysical Journal Letters, 902, L38

Cartwright, R. J., Beddingfield, C. B., Nordheim, T. A., et al. 2020c, The Astrophysical Journal Letters, 898, L22

Cartwright, R. J., Nordheim, T. A., DeColibus, R. A., et al. 2022, The Planetary Science Journal, 3, 8

Cartwright, R. J., Villanueva, G. L., Holler, B. J., et al. 2024, The Planetary Science Journal, 5

Castillo-Rogez, J., Daswani, M., Glein, C., Vance, S., & Cochrane, C. 2022, Geophysical Research Letters, 49, e2021GL097256

Castillo-Rogez, J., Neveu, M., McSween, H. Y., et al. 2018, Meteoritics & Planetary Science, 53, 1820

Castillo-Rogez, J., Weiss, B., Beddingfield, C., et al. 2023, Journal of Geophysical Research: Planets, e2022JE007432

Clark, R. N., Brown, R. H., Cruikshank, D. P., & Swayze, G. A. 2019, Icarus, 321, 791

Clark, R. N., Curchin, J. M., Hoefen, T. M., & Swayze, G. A. 2009, Journal of Geophysical Research: Planets, 114

Clark, R. N., & Lucey, P. G. 1984, Journal of Geophysical Research: Solid Earth, 89, 6341

Clark, R. N., & Roush, T. L. 1984, Journal of Geophysical Research: Solid Earth, 89, 6329

Cohen, I. J., Beddingfield, C., Chancia, R., et al. 2022, The planetary science journal, 3, 58

Cook, J. C., Dalle Ore, C. M., Protopapa, S., et al. 2018, Icarus, 315, 30

Cook, J. C., Protopapa, S., Dalle Ore, C. M., et al. 2023, Icarus, 389, 115242

Cooke, I. R., Fayolle, E. C., & Öberg, K. I. 2016, The Astrophysical Journal, 832, 5

Cruikshank, D., Pilcher, C. B., & Morrison, D. 1977, The Astrophysical Journal, 217, 1006
Dartois, E. 2011, Icarus, 212, 950
Dartois, E., Deboffle, D., & Bouzit, M. 2010, Astronomy & Astrophysics, 514, A49
de Pra, M., Hénault, E., Pinilla-Alonso, N., et al. 2024
De Sanctis, M. C., Raponi, A., Ammannito, E., et al. 2016, Nature, 536, 54
DeColibus, R. A., Chanover, N. J., & Cartwright, R. J. 2022, The Planetary Science Journal, 3, 119
—. 2023, The Planetary Science Journal, 4, 191
Delitsky, M. L., & Lane, A. L. 1998, Journal of Geophysical Research: Planets, 103, 31391
Eiler, J. M., Kitchen, N., & Rahn, T. A. 2000, Geochimica et Cosmochimica Acta, 64, 733
Emery, J., Wong, I., Brunetto, R., et al. 2024, Icarus, 116017
Escribano, R. M., Muñoz Caro, G. M., Cruz-Diaz, G. A., Rodríguez-Lazcano, Y., & Maté, B. 2013, Proceedings of the National Academy of Sciences, 110, 12899
Fray, N., & Schmitt, B. 2009, Planetary and Space Science, 57, 2053
Fujiya, W., Kawasaki, N., Nagashima, K., et al. 2023, Nature Geoscience, 16, 675
Gerakines, P., & Moore, M. 2001, Icarus, 154, 372
Gerakines, P., Moore, M. H., & Hudson, R. L. 2000, Astronomy and Astrophysics, v. 357, p. 793-800 (2000), 357, 793
Gerakines, P. A., & Hudson, R. L. 2020, The Astrophysical Journal, 901, 52
Gerakines, P. A., Materese, C. K., & Hudson, R. L. 2023, Monthly Notices of the Royal Astronomical Society, 522, 3145
Gerakines, P. A., Yarnall, Y. Y., & Hudson, R. L. 2022, Monthly Notices of the Royal Astronomical Society, 509, 3515
Glein, C. R., Baross, J. A., & Waite Jr, J. H. 2015, Geochimica et Cosmochimica Acta, 162, 202
Glein, C. R., & Waite Jr, J. H. 2018, Icarus, 313, 79
Glein, C. R., Grundy, W. M., Lunine, J. I., et al. 2024, Icarus, 115999
Grim, R., Greenberg, J., De Groot, M., et al. 1989, Astronomy and Astrophysics Supplement Series (ISSN 0365-0138), vol. 78, no. 2, May 1989, p. 161-186., 78, 161
Grundy, W., Schmitt, B., & Quirico, E. 2002, Icarus, 155, 486
Grundy, W., Young, L., Spencer, J., et al. 2006, Icarus, 184, 543
Grundy, W., Young, L., & Young, E. 2003, Icarus, 162, 222
Grundy, W., Binzel, R., Buratti, B., et al. 2016, Science, 351, aad9189
Grundy, W., Tegler, S., Steckloff, J., et al. 2024a, Icarus, 410, 115767
Grundy, W., Wong, I., Glein, C., et al. 2024b, Icarus, 411, 115923
Hage, W., Liedl, K. R., Hallbrucker, A., & Mayer, E. 1998, Science, 279, 1332
Hanel, R., Conrath, B., Flasar, F., et al. 1986, Science, 233, 70
Hansen, G. B. 1997, Advances in Space Research, 20, 1613
—. 2005, Journal of Geophysical Research: Planets, 110
Hapke, B. 2012, Theory of reflectance and emittance spectroscopy (Cambridge university press)
Haynes, W. M. 2016, CRC handbook of chemistry and physics (CRC press)
Hendrix, A. R., Hurford, T. A., Barge, L. M., et al. 2019, Astrobiology, 19, 1
Hexter, R. 1958, Spectrochimica Acta, 10, 281
Hibbitts, C., Klemaszewski, J., McCord, T., Hansen, G., & Greeley, R. 2002, Journal of Geophysical Research: Planets, 107, 14
Hibbitts, C., McCord, T., & Hansen, G. 2000, Journal of Geophysical Research: Planets, 105, 22541
Holler, B., Young, L., Grundy, W., & Olkin, C. 2016, Icarus, 267, 255
Hudson, R., Moore, M., & Gerakines, P. 2001, The Astrophysical Journal, 550, 1140
Jakobsen, P., Ferruit, P., de Oliveira, C. A., et al. 2022, Astronomy & Astrophysics, 661, A80
Johnson, R., Carlson, R., Cooper, J., et al. 2004, Jupiter: The Planet, Satellites and Magnetosphere, 485
Kirchoff, M. R., Dones, L., Singer, K., & Schenk, P. 2022, The Planetary Science Journal, 3, 42
Leonard, E. J., Elder, C., Nordheim, T. A., et al. 2021, The Planetary Science Journal, 2, 174
Licandro, J., Pinilla-Alonso, N., Holler, B., et al. 2023
Mamo, B., Brody, J., Teolis, B., et al. 2023in , 220–08
Mastrapa, R., Sandford, S., Roush, T., Cruikshank, D., & Dalle Ore, C. 2009, The Astrophysical Journal, 701, 1347
McClure, M. K., Rocha, W., Pontoppidan, K., et al. 2023, Nature astronomy, 1
McCord, T. a., Hansen, G., Clark, R., et al. 1998, Journal of Geophysical Research: Planets, 103, 8603
Menten, S. M., Sori, M. M., & Bramson, A. M. 2024, XXXX, XX, XXX
Mifsud, D. V., Kaňuchová, Z., Ioppolo, S., et al. 2022, Journal of Molecular Spectroscopy, 385, 111599
Milkov, A. V., & Etiope, G. 2018, Organic geochemistry, 125, 109

Mogan, S. R. C., Tucker, O. J., Johnson, R. E., Sreenivasan, K. R., & Kumar, S. 2020, Icarus, 352, 113932
Moore, J. M., Chapman, C. R., Bierhaus, E. B., et al. 2004a, jpsm, 1, 397
Moore, M., Hudson, R., & Ferrante, R. 2004b, The First Decadal Review of the Edgeworth-Kuiper Belt, 291
Moore, M., & Khanna, R. 1991, Spectrochimica Acta Part A: Molecular Spectroscopy, 47, 255
Moore, M. H., Ferrante, R., Hudson, R., & Stone, J. 2007, Icarus, 190, 260
Mumma, M. J., & Charnley, S. B. 2011, Annual Review of Astronomy and Astrophysics, 49, 471
National Academies of Sciences, Engineering, and Medicine. 2022
Ness, N. F., Acuna, M. H., Behannon, K. W., et al. 1986, Science, 233, 85
Neveu, M., Desch, S. J., Shock, E. L., & Glein, C. R. 2015, Icarus, 246, 48
Newman, S., Buratti, B., Jaumann, R., Bauer, J., & Momary, T. 2007, The Astrophysical Journal, 670, L143
Nordheim, T., Hand, K. P., Paranicas, C., et al. 2017, Icarus, 286, 56
Palumbo, M., Strazzulla, G., Pendleton, Y., & Tielens, A. 2000, The Astrophysical Journal, 534, 801
Peter, J. S., Nordheim, T. A., & Hand, K. P. 2024, Nature Astronomy, 8, 164
Pinilla-Alonso, N., Bannister, M., Brunetto, R., et al. 2021, JWST Proposal. Cycle 1, 2418
Pinto, O. H., Kelley, M., Villanueva, G., et al. 2023, The Planetary Science Journal, 4, 208
Postberg, F., Kempf, S., Schmidt, J., et al. 2009, Nature, 459, 1098
Postberg, F., Sekine, Y., Klenner, F., et al. 2023, Nature, 618, 489
Protopapa, S., Cook, J., Grundy, W., et al. 2020, Pluto System after New Horizons
Protopapa, S., Raut, U., Wong, I., et al. 2024, Nature Communications
Quirico, E., & Schmitt, B. 1997a, Icarus, 127, 354
—. 1997b, doi: https://doi.org/10.26302/SSHADE/EXPERIMENT_BS_20130215_001
Raponi, A., De Sanctis, M. C., Carrozzo, F. G., et al. 2019, Icarus, 320, 83
Rauscher, B. J. 2023, doi: https://arxiv.org/abs/2306.03250
Raut, U., & Baragiola, R. 2013, The Astrophysical Journal, 772, 53
Raut, U., Fulvio, D., Loeffler, M., & Baragiola, R. 2012, The Astrophysical Journal, 752, 159
Rivkin, A., Volquardsen, E., & Clark, B. 2006, Icarus, 185, 563
Rouleau, F., & Martin, P. 1991, The Astrophysical Journal, 377, 526
Sandford, S., Allamandola, L., Tielens, A., & Valero, G. 1988, Astrophysical Journal, Part 1 (ISSN 0004-637X), vol. 329, June 1, 1988, p. 498-510., 329, 498
Smith, B. A., Soderblom, L., Beebe, R., et al. 1986, Science, 233, 43
Sori, M. M., Bapst, J., Bramson, A. M., Byrne, S., & Landis, M. E. 2017, Icarus, 290, 1
Souza-Feliciano, A., Holler, B., Pinilla-Alonso, N., et al. 2024, Astronomy & Astrophysics, 681, L17
Steckloff, J. K., Goldstein, D., Trafton, L., Varghese, P., & Prem, P. 2022, Icarus, 384, 115092
Strazzulla, G., Brucato, J., Palumbo, M., & Spinella, F. 2007, MEMORIE-SOCIETA ASTRONOMICA ITALIANA, 78, 681
Taylor, J. 1997, Introduction to error analysis, the study of uncertainties in physical measurements
Tegler, S., Grundy, W., Loeffler, M., et al. 2024, The Planetary Science Journal, 5, 31
Tosi, F., Mura, A., Cofano, A., et al. 2024, Nature Astronomy, 8, 82
Villanueva, G., Hammel, H., Milam, S., et al. 2023, Science, 381, 1305
Wong, I., Hines, D., Brunetto, R., et al. 2023in , 401–08
Wong, I., Brown, M. E., Emery, J. P., et al. 2024, The Planetary Science Journal, 5, 87

APPENDIX

A1. *Data and Methods: NIRSpec Observations*

Data processing utilized the Science Calibration Pipeline v1.13.4 with CRDS context jwst_1214.pmap to process raw *uncal* data into *s3d* spectral cubes for each of the four dithers (Bushouse et al. 2023). The pipeline was run using the default parameters and including the NSClean routine to remove the $1/f$ pattern noise (Rauscher 2023). The spectral extraction used a "template PSF-fitting" routine. The wavelength grid was first computed using the *CRVAL3* and *CRDELT3* header keywords, with each wavelength corresponding to a specific slice in the data cube. An initial by-eye estimate was made for the centroid position of the target (Ariel is a point source given the $0.1''$ NIRSpec pixels). The background was then calculated as the median of all pixels >5 pixels from the centroid and subtracted from all pixels in the slice. The "template PSF" was then calculated by taking the median of a moving 21-slice window. A 9×9 pixel box was cut out around the centroid of the template PSF, normalized to unity within the box, and iteratively fit to the slice in the middle of the 21-slice window using the *scipy.optimize.minimize* function and the Nelder-Mead algorithm. The two fit parameters were the flux scaling factor and the background, which were used to construct the best-fit model. The 1D spectrum was constructed by extracting the flux within a 3.5-pixel radius circular aperture, centered on the centroid in each slice. To remove the solar component, the four dithers were medianed and then divided by a median G395M spectrum of P330E, a well-established spectrophotometric calibration star (G2V, Vmag 13.028 ± 0.004; e.g., Bohlin & Landolt 2015). The individual P330E spectra were computed using the same template PSF-fitting routine described above. Uncertainties for the Ariel and P330E spectra were computed as the median absolute deviation within each wavelength bin, with the uncertainties propagated to the final P330E-divided spectra (Figure 1).

A2. *Data and Methods: Radiative Transfer Modeling*

The synthetic spectra reported in this study were generated by adopting Mie scattering theory (e.g., Bohren & Huffman 1983) to calculate the single scattering albedo ($\bar{\omega}_0$) for each component using their real, n, and imaginary, k, parts of the complex refractive index, derived from laboratory experiments for crystalline CO_2 ice (150 K, Hansen 1997; 70 K, Gerakines & Hudson 2020; 21 K Quirico & Schmitt 1997a,b), CO ice (Robert Brown, private communication; 20 K, Gerakines et al. 2023), crystalline H_2O ice (80 K; Mastrapa et al. 2009), and amorphous carbon (room temperature; Rouleau & Martin 1991). These $\bar{\omega}_0$ values were then passed to Hapke equations that calculate geometric albedo as a function of wavelength (Hapke 2012). The program generates one-layer models of end-member species (like those shown in Figure 2) or particulate or areal mixtures of various components (Figure A1). Minor resonances in synthetic spectra generated using Mie-derived $\bar{\omega}_0$ are addressed by calculating albedo using a range of grain sizes (± 10% spread in diameters), which are then averaged at each wavelength step in the final model. Although Mie scattering theory only approximates the structure of planetary regoliths, it is widely used in radiative transfer models to simulate the surfaces of icy bodies. More details and caveats on this program and its prior application to simulate the spectral properties of the Uranian moons' surfaces are provided in, e.g., Cartwright et al. 2023.

A3. *Results and Analyses: Comparison between Ariel's 4.90 μm Band and Radiolytically Formed CO_3*

Here we report laboratory spectra of radiolytically generated CO_3 compared to Ariel's 4.90 μm band (Figure A2).

A4. *Results and Analyses: Ariel's CO_2 scattering peak compared to the indices of refraction for CO_2*

Here we report an arbitrarily scaled NIRSpec spectrum of Ariel's trailing hemisphere compared to the indices of refraction for CO_2, measured by Gerakines & Hudson 2020 (Figure A3).

A5. *Results and Analyses: Ariel trailing / Ariel leading spectral ratio*

Here we report a ratio between the spectra collected over Ariel's trailing and leading hemispheres (Figure A4).

A6. *Results and Analyses: H_2O_2 and Ariel's 3.6 μm Feature*

To investigate whether H_2O_2 is present on Ariel and to measure its 3.6 μm feature, we fitted fourth-order polynomial models to the spectra of Ariel's leading and trailing hemispheres between 3.45 and 3.7 μm and measured the resulting continuum-subtracted features (Figure A5). We find no evidence for the 3.505 μm H_2O_2 feature detected on Europa (e.g., Carlson et al. 1999), Enceladus (Newman et al. 2007), and Charon (Protopapa et al. 2024) (Figure A5). The

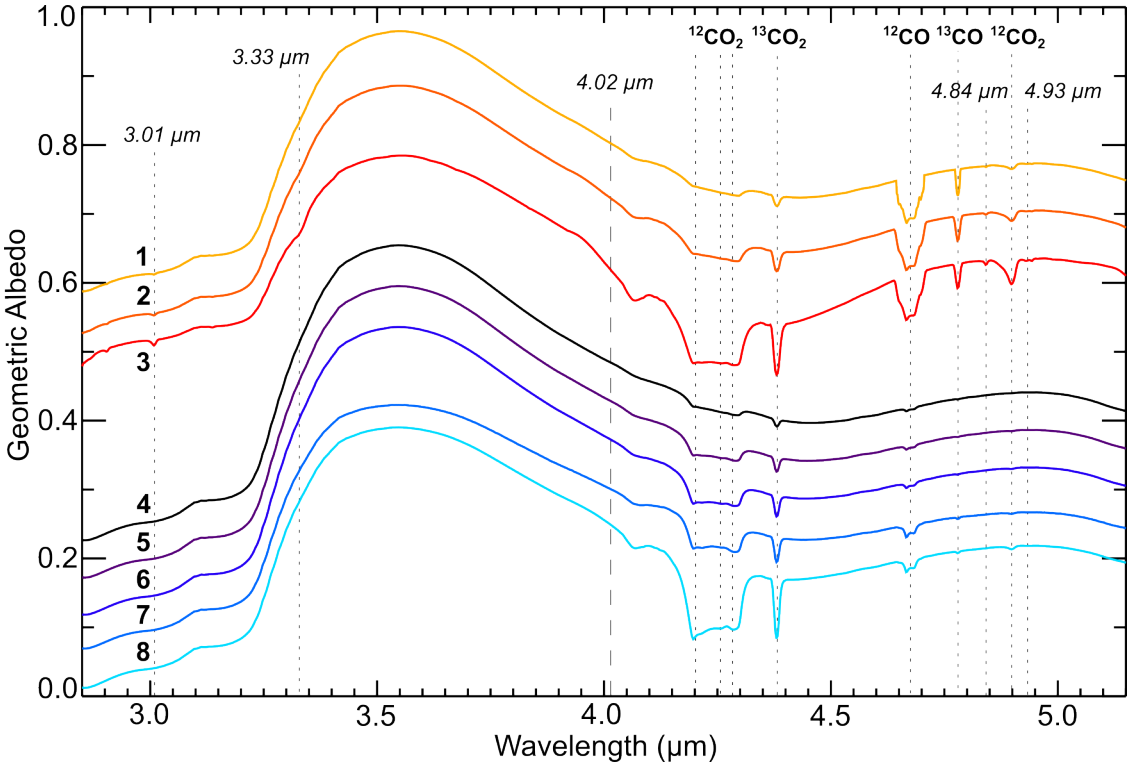

Figure A1. *Synthetic spectra (section A2) comprised of areal (models 1-3) and particulate (models 4-8) mixtures, offset vertically for clarity. These spectral models include crystalline H_2O ice (Mastrapa et al. 2009), crystalline CO_2 ice (Quirico & Schmitt 1997a,b), crystalline CO ice (Robert Brown, private communication), and amorphous carbon (Rouleau & Martin 1991), with grain diameters of 2, 10, 10, and 1 μm, respectively. Each model includes 10% CO ice and 0.5% amorphous carbon mixed with: (1) 84.5% H_2O ice and 5% CO_2 ice; (2) 79.5% H_2O ice and 10% CO_2 ice; (3) 64.5% H_2O ice and 25% CO_2 ice; (4) 64.5% H_2O ice and 25% CO_2 ice; (5) 49.5% H_2O ice and 40% CO_2 ice; (6) 39.5% H_2O ice and 50% CO_2 ice; [a] (7) 14.5% H_2O ice and 75% CO_2 ice; (8) 14.5% H_2O ice and 75% CO_2 ice. [a] Model 7 includes 25% CO_2 (Quirico & Schmitt 1997a; 10 μm grains) and 50% CO_2 (Gerakines & Hudson 2020; 100 μm grains). These models demonstrate that the Ariel features between 4.19 and 4.30 μm and 4.65 and 4.80 μm, which are associated with the ν_3 modes of CO_2 and CO ice, respectively, are exhibited by all eight models (dotted lines with bold text). In contrast, weak CO_2 features tentatively observed on Ariel, near 3.01 μm, 3.33 μm, 4.84 μm, and 4.93 μm (dotted lines, italicized text), are only exhibited by areal mixtures that include ≥10% CO_2 (models 2-3), and are not observed in any of the particulate mixtures (25 – 75% CO_2 ice; models 4-8). The 4.90 μm band is expressed by all areal mixtures (5 – 25% CO_2, models 1-3) and particulate mixtures with ≥40% CO_2 (models 5-8). The presence of weak CO_2 ice features in the areal mixtures, and their absence from the particulate models, demonstrates that concentrated deposits of pure CO_2 on Ariel's surface are required for these features to be expressed (section 4.1). None of the areal or particulate mixtures exhibit a ∼4 μm feature, suggesting that carbonates, or another component, contribute to Ariel's 4.02 μm band (dashed line, italicized text).*

continuum-subtracted data show weak features centered near 3.55 and 3.60 μm on Ariel's trailing hemisphere. Whether these two features result from different species or are two subtle lobes of the same component is difficult to discern. We consider candidate species for the 3.55 μm and 3.60 μm features in section A7.

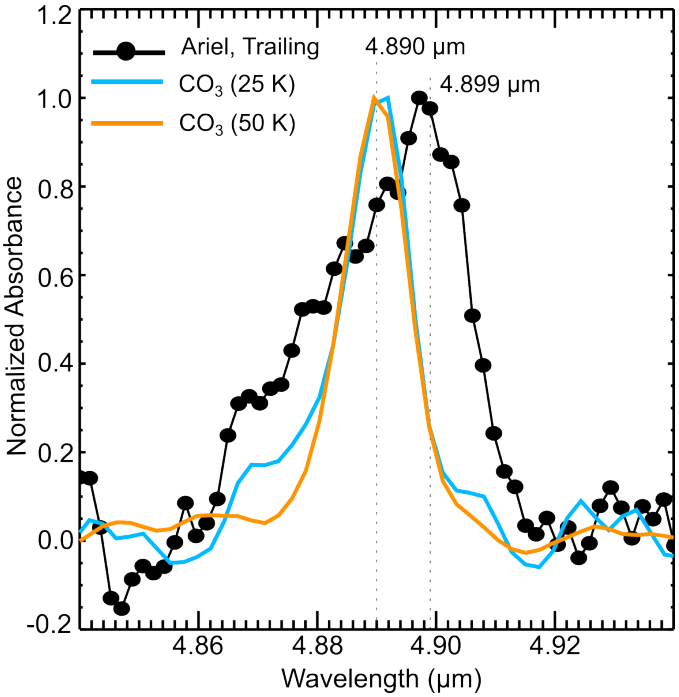

Figure A2. *Comparison between a continuum-divided version of Ariel's 4.90 μm band on its trailing hemisphere and a 4.89 μm CO_3 band generated via irradiation of CO_2 ice thin film with 100 keV H^+ protons, scaled in optical depth units (-ln(R/R_0), where R is the reflectance of the film and gold substrate and R_0 is the reflectance of the bare gold substrate (Raut & Baragiola 2013)). All spectra are normalized to one at their maxima. The offset between the CO_3 features and Ariel's 4.90 μm band supports the interpretation that this feature results from collective oscillations across a crystalline CO_2 ice lattice (Bini et al. 1991) (Figure 2). It is possible that radiolytically produced CO_3 contributes to the broad short-wavelength side of Ariel's 4.90 μm band. However, additionally experiments are required to determine whether this broadening of Ariel's 4.90 μm band results from mixing with CO_3 or other variables such as the temperature of CO_2 on Ariel.*

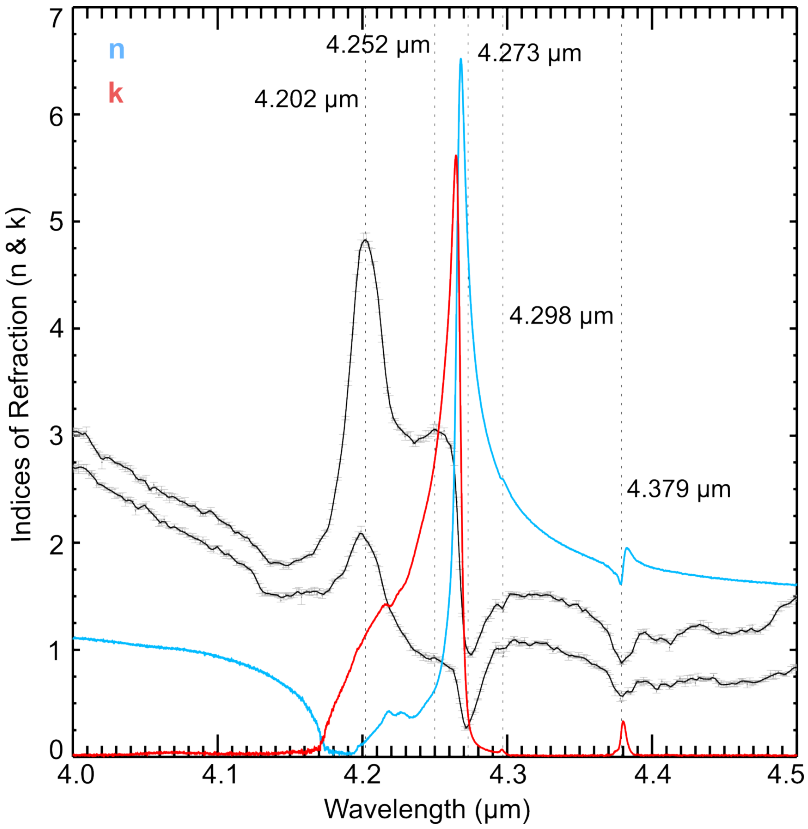

Figure A3. *The real 'n' (blue) and imaginary 'k' (red) complex refractive indices for crystalline CO_2 ice measured in the laboratory at 70 K (Gerakines & Hudson 2020) compared to arbitrarily scaled spectra (1σ errors) of Ariel's leading and trailing (offset upward for clarity) hemispheres. Dashed lines indicate spectral features identified on Ariel that result from $^{12}CO_2$ and $^{13}CO_2$ ice and correspond to changes in n and k as a function of wavelength. Ariel's $^{12}CO_2$ scattering peak starts close to 4.175 μm, where k substantially increases above n, and ends near 4.265 μm, where k drops off steeply and n increases above 6. The 4.30 μm $^{16}O^{12}C^{18}O$ and 4.38 μm $^{13}CO_2$ features coincide with small increases in k above zero and slight dips in n.*

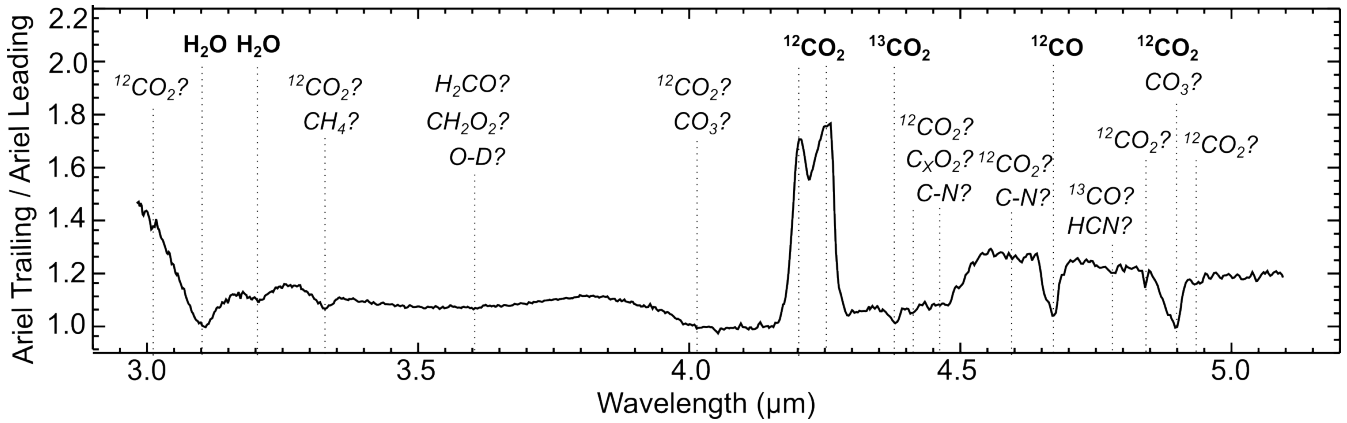

Figure A4. *Ratio between Ariel's trailing and leading hemispheres, normalized to 1 at 4 μm. Dashed lines highlight the spectral features identified in the Ariel data (Figure 1) that show notable trailing/leading hemispherical asymmetries, including subtle features near 3.33, 4.84, and 4.93 μm that could result from deposits of CO_2 ice upward of ∼10 mm thick (section 4.1, Figure 4). Candidate species are described in section A7.*

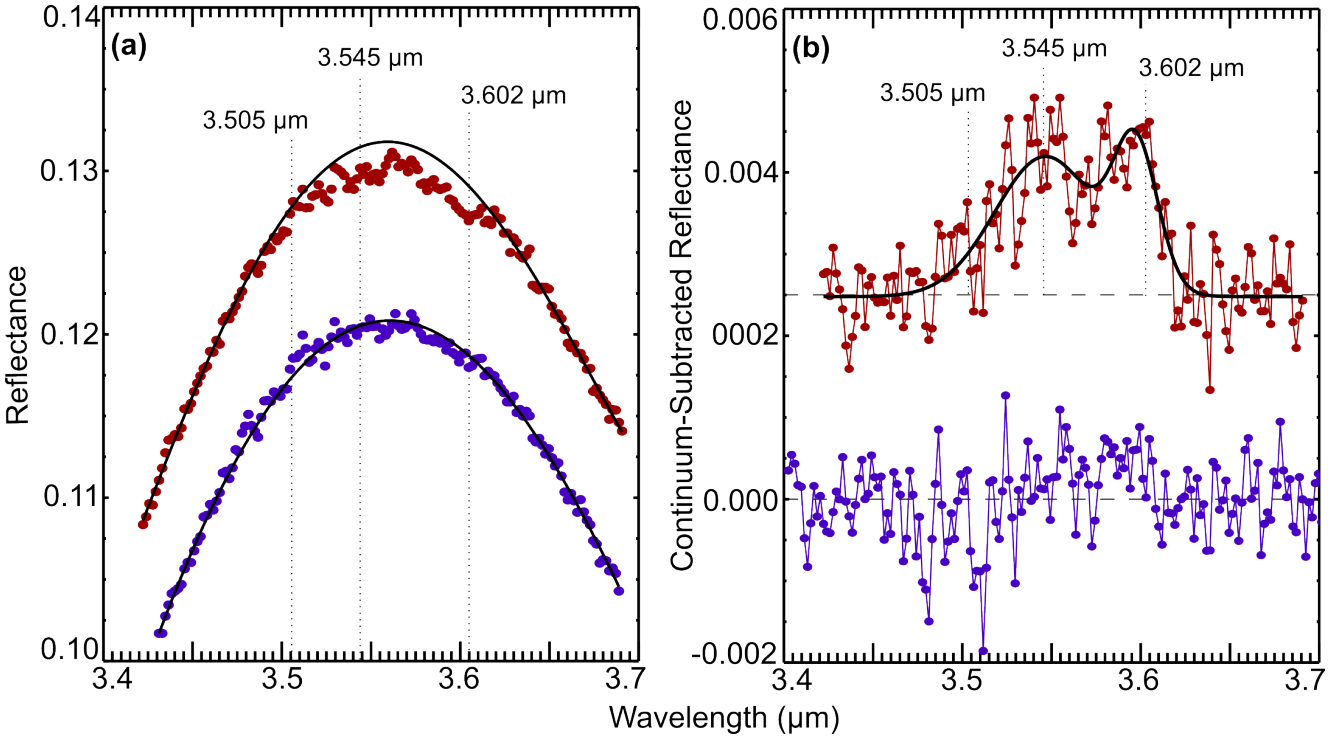

Figure A5. *left: Spectra of Ariel's leading (purple) and trailing (red) hemispheres, scaled to arbitrary reflectance, fit by fourth-order polynomials simulating their continua. Dashed lines highlight the central wavelength position of H_2O_2 measured in the laboratory (3.505 μm) and two other subtle features centered near 3.545 μm and 3.602 μm. Right: Continuum-subtracted spectra of Ariel's leading (purple) and trailing (red, offset upwards by 0.0025) hemispheres, spanning the 3.4 to 3.7 μm wavelength range. A two-Gaussian model (black) has been fit to the weak 3.55 and 3.60 μm features observed on Ariel's trailing hemisphere that are not seen on its leading hemisphere. Neither spectrum exhibits a 3.505 μm band resulting from a H_2O_2 combination mode ((Bain & Giguère 1955).*

A7. *Discussion: Candidate Constituents*

Of the fifteen features we identified and measured, seven are confidently attributed to H_2O, $^{12}CO_2$, or ^{12}CO (Table 1). The other eight are centered near 3.33, 4.02, 4.15, 4.30, 4.41, 4.47, 4.59, and 4.78 μm. The 3.33 μm and 4.15 μm features are likely dominated by CO_2, but the 3.33 μm feature may include species exhibiting C-H stretching modes (e.g., Clark et al. 2009; Grundy et al. 2002; Dartois et al. 2010), whereas the 4.15 μm feature may also include contributions from deuterated water ice (D_2O/HDO; Clark et al. 2019).

Ariel's 4.02 μm feature might result from a broad $\nu_1 + \nu_3$ combination mode expressed by CO_3-bearing minerals (Hexter 1958; Bishop et al. 2021). Additionally, S-bearing species have been suggested to explain Callisto's broad 4.02 μm feature, including disulfanide (HS_2^-) and hydrogen disulfide (H_2S_2; (Cartwright et al. 2020b), or perhaps even a wavelength shifted sulfur dioxide (SO_2) band (e.g., McCord et al. 1998). H_2CO_3, formed via irradiation of H_2O mixed with CO_2, expresses a broad band between 3.8 and 3.9 μm due to the CO_3^{-1} anion (e.g., Hage et al. 1998) that might contribute to Ariel's 4.02 μm, assuming some process is able to shift its band center closer to 4 μm. Conversely, Ariel's 4.02 μm feature might be associated with the Christiansen band exhibited by $^{12}CO_2$ ice near 4.07 μm (seen in the CO_2 spectral models 1-3 shown in Figures 2 and A1). However, there is a sizeable wavelength gap ($\sim$0.05 μm) between the Christiansen features displayed by these spectral models and Ariel's 4.02 μm band, and it is uncertain why the Christiansen band would exhibit such a large shift, especially given that the feature is not shifted in spectra of CO_2-rich TNOs (Figure A6).

Because of the strength of H_2O ice absorption, and the shape of the H_2O ice continuum in the 4 μm wavelength range, exact identification of Ariel's 4.02 μm band center is difficult, and it may be centered at slightly shorter wavelengths, between 3.98 and 4 μm. Similarly, Ceres exhibit a 4 μm feature that shifts between 3.95 and 4.02 μm, with Mg-Ca carbonates shifting its 4 μm feature to the global average of 3.95 μm and Na carbonates shifting the band feature to 4.02 μm (e.g., Carrozzo et al. 2018). Therefore, if Ariel's 4.02 μm band is in reality centered at slightly shorter wavelengths, it could still be consistent with the broad $\nu_1 + \nu_3$ combination mode expressed by carbonate minerals.

Ariel's 4.30 μm feature is embedded on the long-wavelength end of its 4.27 μm $^{12}CO_2$ ice band and probably results from the CO_2 isotopologue $^{16}O^{12}C^{18}O$ (Bennett et al. 2010b). Although amorphous CO_2 could hypothetically contribute to Ariel's 4.30 μm band, it is not expected to be present at Ariel's peak surface temperatures (e.g., Escribano et al. 2013).

The 4.41 μm and 4.47 μm features could result from irradiation of CO and CO_2 mixtures, forming C_3O_2 and other higher-order carbon chain oxides (e.g., Gerakines & Moore 2001; Strazzulla et al. 2007). Alternatively, these two features could result from irradiation of carbon oxides and ammonia (NH_3), forming CN-bearing compounds (e.g., Strazzulla et al. 2007). The 4.41 μm feature might also (in part) result from $^{16}O^{13}C^{18}O$ ice (Bennett et al. 2010b).

Ariel's 4.59 μm feature could result from irradiation of H_2O, CO_2, and NH_3, forming OCN^-, a key tracer of nitrogen-bearing species in the interstellar medium and protoplanetary disks (e.g., McClure et al. 2023). If OCN^- is confirmed, then a complementary NH_4^+ feature should be present near 6.85 μm (e.g., Grim et al. 1989; Palumbo et al. 2000; Bennett et al. 2010a).

Ariel's 4.78 μm band most likely results from ^{13}CO (e.g., Bennett et al. 2010b), given that it is only detected on Ariel's trailing side, where the ^{12}CO feature is dramatically stronger (see section A8 for discussion of $^{13}CO/^{12}CO$ isotopic ratios). Nonetheless, the ν_3 mode of hydrogen cyanide ice (HCN; e.g., Gerakines et al. 2022) might contribute to this feature as well, if nitriles are present.

Subtle features near 3.55 and 3.60 μm on Ariel's trailing side (Figure A5) may result from irradiation of CO_2 and H_2O, possibly generating formaldehyde (H_2CO; Moore et al. 2004b), formic acid (CH_2O_2; Bisschop et al. 2007), or perhaps oxalates (C_2O_4; Applin et al. 2016). A 3.6 μm feature on Saturn's moon Phoebe has also been attributed to HDO/D_2O ice (Clark et al. 2019), and perhaps deuterated water ice contributes to Ariel's 3.6 μm feature as well.

Finally, we identified, but did not measure, three other very subtle features centered near 3.01, 4.84, and 4.93 μm on Ariel's trailing hemisphere, which probably result from CO_2 (Figures 4 and A4; Hansen 1997; Quirico & Schmitt 1997a).

Disentangling these various components requires follow-up laboratory experiments and associated modeling efforts. In particular, there is a need to determine whether NH_3 on Ariel may have been radiolytically converted into nitriles, thereby explaining the absence of N-H stretching modes in the NIRSpec data reported here. Additionally, Ariel's prominent double-lobed scattering peaks near 4.20 and 4.25 μm share morphological similarities to double-lobed CO_2 gas emission peaks detected at Callisto (Carlson 1999), and more recently, the Centaur 39P/Oterma (Pinto et al. 2023). However, there is a notable wavelength shift between these CO_2 gas emission peaks ($\sim$4.2 – 4.3 μm), and

Ariel's scattering peaks (4.16 – 4.26 μm), which is more consistent with scattering within a thick layer of CO_2 ice (Model 3 in Figure 2; Figure A3).

A8. *Discussion: Comparison between Ariel and CO_2-bearing TNOs*

Here we compare NIRSpec data of Ariel's leading and trailing hemispheres to spectra of three TNOs observed as part of General Observer program 2418 (Pinilla-Alonso et al. 2021). These TNOs are representative of the three spectral types identified by this program (de Pra et al. 2024).

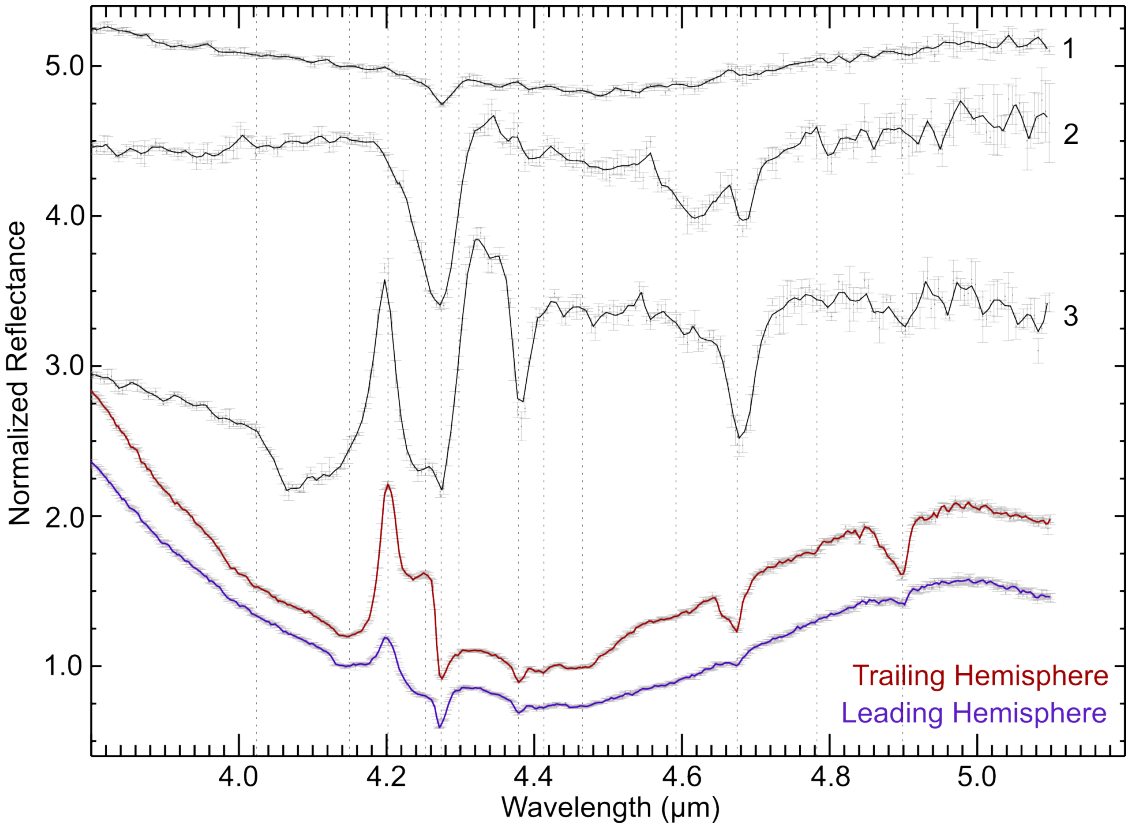

Figure A6. *Comparison between NIRSpec IFU spectra and 1σ uncertainties for Ariel's leading (purple) and trailing (red) hemispheres and the TNOs 47171 Lempo (1999 TC36) (1), 2013 LU28 (2), and 2004 XA192 (3), selected to represent members of the ''bowl,' 'cliff,' and 'double-dip' TNOs types (Pinilla-Alonso et al. 2021; de Pra et al. 2024), respectively. All spectra are normalized to 1 at 4.15 μm and offset vertically for clarity. Similar to other double-dip TNOs, 2004 XA192 exhibits strong $^{12}CO_2$ and $^{13}CO_2$ bands, with a CO_2 scattering peak similar to Ariel's 4.202 μm peak. However, none of the TNOs display a strong 4.252 μm peak, unlike Ariel. 2004 XA192 also exhibits a strong ~4.07 μm band resulting from the Christiansen effect, where n=1 and k=0 in crystalline CO_2 ice (Figure A3). This Christiansen band is notably absent from the Ariel spectra and synthetic spectra composed of large grain sizes (diameters ~100 μm; Gerakines & Hudson 2020), generated using our Hapke-Mie approach (section A2).*

A9. *Discussion: $^{13}CO/^{12}CO$ isotopic ratios*

Prior studies have used remotely sensed H_2O, HDO/D_2O ice, $^{12}CH_4$, $^{13}CH_4$, $^{12}CH_3D$, $^{13}CO_2$, and $^{12}CO_2$ spectral features to estimate D/H and $^{13}C/^{12}C$ isotopic ratios and gain insight into the formation conditions for different icy bodies and possible endogenic sources of material on their surfaces (Clark et al. 2019; Grundy et al. 2024b; Glein et al. 2024; Cartwright et al. 2024). Ariel's strong $^{12}CO_2$ scattering peaks makes reliable determination of its $^{13}CO_2/^{12}CO_2$ isotopic ratios difficult from analysis of ν_3 band parameters for $^{12}CO_2$, and we did not attempt to retrieve a $^{12}CO_2$ abundance from other spectral features (e.g., at 4.90 μm). However, using the 4.67 μm ^{12}CO and 4.78 μm (likely) ^{13}CO bands detected on Ariel's trailing hemisphere, we calculated $^{13}CO/^{12}CO$ band area and depth ratios of 0.045 $\pm$ 0.010 and 0.146 $\pm$ 0.023, respectively. These results are comparable to Phoebe's $^{13}CO_2/^{12}CO_2$ band area (0.059

± 0.005) and depth (0.186 ± 0.036) ratios (Cartwright et al. 2024), and the ratios on Ariel's leading hemisphere appear qualitatively to be higher, hinting that Ariel may be significantly enhanced in ^{13}C relative to 'terrestrial' values ($^{13}C/^{12}C \approx 0.010 - 0.012$) exhibited by most bodies in the inner Solar System and Saturn's rings and regular satellites (e.g., Clark et al. 2019). Whether $^{13}C/^{12}C$ ratios derived from CO at Ariel would yield similar results to carbon isotopic ratios derived from CO_2 at Phoebe is uncertain. Furthermore, CO is likely contaminated by CO_2 at Ariel and its 4.78 μm band may be enhanced by HCN ice, assuming nitriles are present, complicating analysis of its carbon isotopes. We report a preliminary analysis of possible ^{13}C enrichment of CO and CO_2 ices on Ariel in Appendix A10. More detailed modeling of Ariel's carbon isotopes and their spectral expression at infrared wavelengths is likely required to corroborate the CO band ratios present here, to convert band ratios to number ratios, and to fully explore their significance, e.g., in terms of formation of its carbon source material (e.g., Cartwright et al. 2024).

A10. *Discussion: Modeling $^{13}CO_2$ Enrichment*

The pronounced 4.38 μm absorption due to $^{13}CO_2$ and high apparent ratios of $^{13}CO/^{12}CO$ (assuming that CO is a radiolytic product of CO_2) provide hints that Ariel's surface CO_2 ice is enriched in ^{13}C, perhaps substantially. Here we seek to outline explanations of how CO_2 could acquire a large ^{13}C enrichment via a balance between production and escape processes. We then consider a different scenario in which there is long-term isotopic fractionation of CO_2 driven only by escape.

Since CO_2 is concentrated on the trailing hemisphere, it may be produced by radiolytically driven oxidation reactions of, e.g., organic compounds. An alternative or complementary source of CO_2 would be outgassing from the interior (e.g., a soda ocean). It may not be essential to specify the nature of the CO_2 source since both options would provide CO_2 with roughly similar C isotope ratios (see below). The exception would be if radiolytic processes result in isotopic fractionation, but high-energy processes are not generally associated with strong isotope effects because they usually lack selectivity. We can formulate two equations for the evolution of CO_2 isotopologues in the surface environment of Ariel:

$$\frac{dN_{44}}{dt} = J_{44} - k_{44}\left[^{12}CO_2\right]_{exob} \tag{1}$$

and

$$\frac{dN_{45}}{dt} = J_{45} - k_{45}\left[^{13}CO_2\right]_{exob} \tag{2}$$

where N represents the number of molecules, subscripts refer to the masses of CO_2 isotopologues, t stands for time, J designates production rate, k represents a rate constant for atmospheric escape, and brackets indicate the number density of the CO_2 isotopologue of interest at the exobase. We adopt the classic concept of the exobase as a dividing line between nominally collisional and collisionless parts of the atmosphere. We wish to explore the simplest case in which a steady state could be established. Equations 1 and 2 then imply that

$$\left(\frac{^{13}CO_2}{^{12}CO_2}\right)_{exob} = \frac{J_{45}/J_{44}}{k_{45}/k_{44}} = \frac{R_{pro}}{\alpha_{esc}} \tag{3}$$

where R_{pro} stands for a ratio characteristic of a given production process, and α_{esc} is a fractionation factor due to CO_2 loss by atmospheric escape.

We treat R_{pro} as a fixed parameter that may assume $^{13}C/^{12}C$ ratios between those measured in primitive organic matter (1/92; Alexander et al. (2007)) and carbonate minerals (1/83; Fujiya et al. (2023)) in carbonaceous chondrites. The former would reflect an organic source of Ariel's CO_2 ice (e.g., carbonaceous dust), while the latter can serve as an analog for carbonate-bearing subsurface fluids that might erupt CO_2. The second value would be inherited from protosolar nebula CO_2 ice that may have been accreted by Ariel at the time of its formation. The overall range of $^{13}C/^{12}C$ ratios considered here encompasses a broad range of primordial carbon isotope ratios observed across the solar system.

We consider CO_2 loss by Jeans escape. This mechanism has the potential to discriminate between species with different masses (hydrodynamic escape and sputtering are other possibilities, but they are less effective than Jeans escape at fractionating isotopes). For Jeans escape,

$$\alpha_{esc} = \sqrt{\frac{44}{45}}\left(\frac{1+\lambda_{45}^{exob}}{1+\lambda_{44}^{exob}}\right)\exp\left(\lambda_{44}^{exob} - \lambda_{45}^{exob}\right), \tag{4}$$

where $\lambda_i^{\rm exob}$ represents the escape parameter of species i at the exobase, as defined below:

$$\lambda_i^{\rm exob} = \frac{GMm_i}{k_{\rm B}T_{\rm exob}r_{\rm exob}}, \tag{5}$$

where $GM = 8.23\text{x}10^{10}$ m^3 s^{-2}; m_i corresponds to the mass of a molecule of species i; $k_B = 1.381 \times 10^{-23}$ kg m^2 s^{-2} K^{-1}; T_{exob} denotes the exobase temperature, which is assumed to be the same as the rest of the atmosphere (as a first-order approximation); and r_{exob} indicates the distance between the exobase and the center of Ariel.

The isotope ratio at the surface can be related to that at the exobase via

$$\left(\frac{^{13}\text{CO}_2}{^{12}\text{CO}_2}\right)_{\rm surf} = \frac{1}{\alpha_{\rm diff}}\left(\frac{^{13}\text{CO}_2}{^{12}\text{CO}_2}\right)_{\rm exob} \tag{6}$$

where α_{diff} denotes an isotope fractionation factor due to molecular diffusion between the surface and exobase. We assume that turbulent mixing is unimportant in Ariel's tenuous atmosphere (i.e., the homopause is always at the surface). For an isothermal atmosphere, the diffusive fractionation factor can be computed using:

$$\alpha_{\rm diff} = \exp\left(\frac{GM\left(m_{45}-m_{44}\right)\left(r_{\rm exob}^{-1}-r_{\rm surf}^{-1}\right)}{k_{\rm B}T_{\rm atm}}\right), \tag{7}$$

where $r_{surf} = 579\text{x}10^3$ m. We introduce T_{atm} as a mean temperature at altitudes between the surface and exobase.

We do not know the location of Ariel's exobase. One possibility is that Ariel has a surface-bound exosphere. We can determine if this is likely by computing the surface pressure (P_{surf}) that would satisfy the following relation:

$$\frac{\pi d_{\rm CO_2}^2 r_{\rm surf}^2 P_{\rm surf}}{GMm_{\rm CO_2}} = 1, \tag{8}$$

where d_{CO2} corresponds to the kinetic diameter of CO_2 (4.53×10^{-10} m; Haynes (2016)). The pressure would need to be $< 2.8 \times 10^{-8}$ Pa for the exobase to be at the surface. If there is a sufficient CO_2 supply (as suggested by the prominent CO_2 features in the JWST data), then we may assume vapor pressure equilibrium to set a constraint on the maximum temperature that permits a surface-bound exosphere. We use Fray & Schmitt (2009)'s equation:

$$\ln p_{\rm CO_2,sat}\,(\text{bar}) = A_0 + \sum_{j=1}^{5} A_j T_{\rm surf}(\text{K})^{-j} \tag{9}$$

where $p_{CO2,sat}$ designates the saturation pressure of CO_2 ice, T_{surf} indicates the surface temperature, $A_0 = 14.76$, $A_1 = -2571$ K, $A_2 = -7.781 \times 10^4$ K^2, $A_3 = 4.325 \times 10^6$ K^3, $A_4 = -1.207 \times 10^8$ K^4, and $A_5 = 1.35 \times 10^9$ K^5. These parameters are applicable to temperatures between 40 and 195 K (Fray & Schmitt 2009). By calculating the saturation pressure as a function of temperature, we find that the left side of Equation 8 is < 1 (meaning the mean free path is longer than the scale height) when $T_{surf} < 71$ K. Hence, the exobase will be at the surface (i.e., the whole atmosphere is an exosphere) when the temperature is below 71 K; in this case, $\alpha_{diff} = 1$ and we can solve Equations 3-6 to determine the $^{13}CO_2/^{12}CO_2$ ratio at the surface of Ariel.

At higher surface temperatures, the exobase will be at higher altitudes. It is not straightforward to simulate the structure of this type of atmosphere; this is an active area of research (Mogan et al. 2020). However, detailed modeling is probably not needed for our application since we lack specific values of the $^{13}CO_2/^{12}CO_2$ ratio on Ariel to explain (see section A8). Instead, we have the more basic goal of exploring the sensitivity of the isotope ratio to unknowns that influence isotopic fractionation. The two parameters of interest here are the exobase altitude and temperature of the atmosphere. In the present treatment, we still assume that the atmosphere is isothermal, but it could have a different temperature than that of the surface. Parameters r_{exob} and T_{atm} in Equation 7 can be varied to assess how much they could change α_{diff}. Equations 3-6 can then be used to estimate the steady-state $^{13}C/^{12}C$ ratio of Ariel's surface CO_2 ice at $T_{surf} \geq 71$ K. We do not account for any carbon isotopic fractionation between CO_2 gas and ice at the surface, as laboratory experiments show that there is no more than ~0.4‰ fractionation down to 130 K (Eiler et al. 2000).

As shown in Figure A7, CO_2 derived from organics or carbonates can be significantly enriched in ^{13}C in the surface environment of Ariel due to atmospheric escape. The predicted enrichment is about 30%, i.e., 300‰. This is very large.

For comparison, biological production of CH_4 from CO_2 is generally considered to have a large isotope effect, with a fractionation that can reach ~80‰ (Milkov & Etiope 2018). Our predictions appear to be qualitatively consistent with the ease of finding features from $^{13}CO_2$ and ^{13}CO in the JWST data. It can be seen in Figure A7 that increasing the exobase altitude may not have a significant effect on the isotope ratio, at least up to 2000 km. The atmospheric temperature can have a larger effect in enriching $^{13}CO_2$ at the surface. Yet, its effect on diffusive fractionation seems less important than Jeans fractionation, which is responsible for most of the total fractionation in our test cases. Isotopic fractionation by diffusion is limited by large scale heights of Ariel's atmosphere.

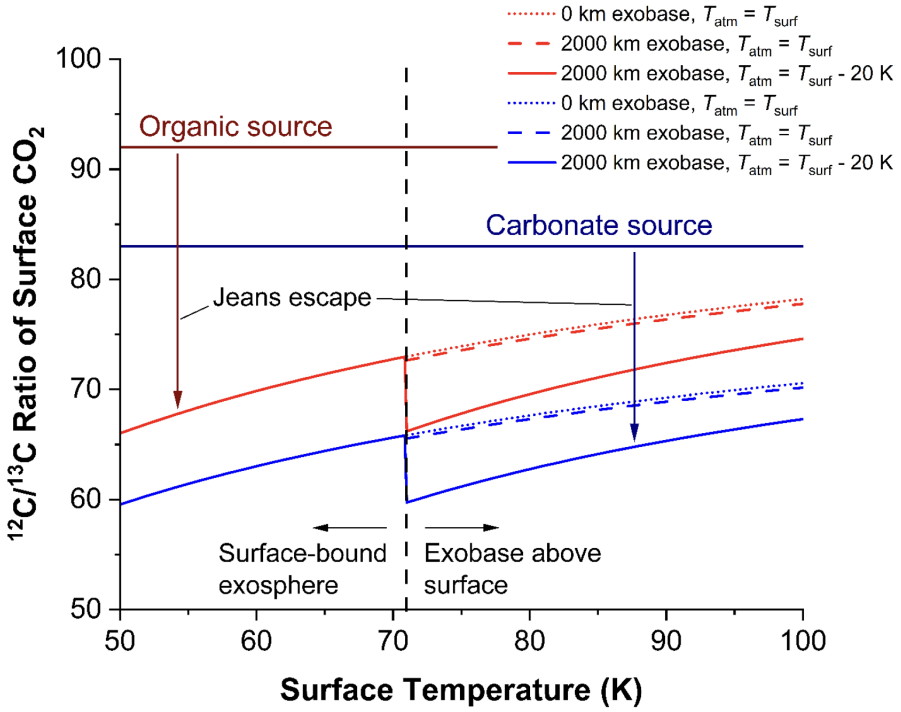

Figure A7. *Carbon isotopic composition (light/heavy) of steady-state CO_2 at the surface of Ariel. These results show how input values of the $^{12}C/^{13}C$ ratio from organics or carbonates (dark horizontal lines) are shifted downward by Jeans escape. For each set of lighter-colored curves, we consider a case with a surface-bound exosphere at all temperatures and $T_{atm} = T_{surf}$ (dotted); a case where the exobase altitude has been increased to 2000 km while keeping $T_{atm} = T_{surf}$ (dashed); and a case where the exobase altitude remains at 2000 km, but the atmospheric temperature is 20 K lower than the surface temperature. The offsets for these cases are intended to be illustrative, and other values are possible.*

The spurious drops at 71 K in Figure A7 arise from the arbitrary assumption that the exobase is at the surface at temperatures below 71 K, and at an altitude of 2000 km at higher temperatures. Although assuming a constant exobase level isolates its effects on the $^{13}C/^{12}C$ ratio, in a more realistic model, the exobase would progressively increase in altitude from the surface level with increasing surface temperature and pressure.

Whether a steady state is reached is an open question. In another end-member scenario, one can assume progressive depletion of a primordial surface CO_2 inventory, as a fraction sublimates each summer to form gaseous CO_2 that undergoes isotopic fractionation due to Jeans escape. From Equation 4, $\alpha_{esc} \approx 0.72$ assuming $T_{surf} = 55$ K and a surface-bound exobase, or 0.78 at $T_{surf} = 71$ K. Assuming escape of a modest fraction $f_{esc} = 0.1$ ppm of all the surface CO_2 each Uranian year, the $^{13}C/^{12}C$ ratio of primordial CO_2 would increase by a factor of $(f_{esc}/\alpha_{esc})\ (4.57\times10^9/86) \approx 7$ (i.e., 7000‰) over the 4.57 Gyr of solar system history, assuming a constant orbital period for Uranus of 86 Earth years. This requires CO_2 to be gaseous for part, and only part, of the Uranian year.

This calculated enrichment in ^{13}C is even more considerable than in the steady-state scenario, as the ever-increasing $^{13}C/^{12}C$ ratio of the surface CO_2 is not diluted by constantly replenishing CO_2 with a canonical $^{13}C/^{12}C \approx 1/90$. This enrichment is of the same order of magnitude as the factors of ≈ 4.5 and 15 inferred, respectively, from the band area and depth ratios of ^{13}CO and ^{12}CO on Ariel (see section A8). The corresponding $f_{esc} = 0.1$ ppm is consistent with an CO_2 initial inventory $(1 + f_{esc})^{4.5e9/86} \approx 200$ times greater than the present-day surface abundance; i.e., equivalent

layer thicknesses on the order of 10 m or larger based on the > 10 mm present-day deposit thicknesses discussed in Section 4.1. Compared to water inventories equivalent to global ice shell thicknesses of 100 km or more (e.g., Castillo-Rogez et al. 2023), this appears compatible with bulk CO_2/H_2O abundance ratios of less than a few mol% based on observations of comets (Mumma & Charnley 2011), which may be indicative of the composition of icy material accreted by Ariel. Such bulk compositions allow for greater values of f_{esc}, which would be required to obtain the same ^{13}C enrichment in intermediate scenarios involving both primordial inventory depletion and some degree of endogenic (and, for CO, radiolytic) replenishment. We leave to future work the questions of what the absolute rate of CO_2 escape might have been through time, whether it is consistent with the removal of almost all of Ariel's surface CO_2 inventory, and how much radiolytic production may be implied to account for trailing vs. leading hemisphere differences in the apparent abundance of CO_2. Future constraints on the $^{18}O/^{16}O$ ratio may enable further discrimination between steady-state and limited replenishment scenarios, as the larger mass difference between $^{16}OC^{18}O$ and $^{16}OC^{16}O$ can be expected to magnify the degree of fractionation.

The models outlined above may have more general applicability to other outer solar system bodies with abundant $^{13}CO_2$. In addition to the phenomena considered in this appendix, it may be useful to consider how lateral heterogeneities in the availability of CO_2 ice, seasonal effects on surface temperatures, kinetic inhibition of CO_2 sublimation, and possible vapor pressure isotope effects at low temperatures might come together to create a rich isotope geochemistry that we are just beginning to glimpse.